The Role of Rough Topography in Mediating Impacts of Bottom Drag in Eddying Ocean Circulation Models

David S. Trossman*

Goddard Earth Sciences Technology and Research, Greenbelt, Maryland, USA

Department of Earth and Planetary Sciences, Johns Hopkins University, Baltimore, Maryland, USA

Department of Earth and Environmental Sciences, University of Michigan, Ann Arbor, USA

Brian K. Arbic

Department of Earth and Environmental Sciences, University of Michigan, Ann Arbor, USA

David N. Straub

Department of Atmospheric and Oceanic Sciences, McGill University, Montreal, CAN

James G. Richman

Center for Ocean-Atmospheric Prediction Studies, Florida State University, Tallahassee, USA

Eric P. Chassignet

Center for Ocean-Atmospheric Prediction Studies, Florida State University, Tallahassee, USA

Alan J. Wallcraft

Oceanography Division, Naval Research Laboratory (NRL-SSC), Stennis Space Center, Mississippi, USA

Xiaobiao Xu

Center for Ocean-Atmospheric Prediction Studies, Florida State University, Tallahassee, USA

∗*Corresponding author address:* NASA Goddard Space Flight Center, Code 610.1, Greenbelt, MD 20771 USA

E-mail: david.s.trossman@nasa.gov

ABSTRACT

Motivated by the substantial sensitivity of eddies in two-layer quasi-geostrophic (QG) turbulence models to the strength of bottom drag, this study explores the sensitivity of eddies in more realistic ocean general circulation model (OGCM) simulations to bottom drag strength. The OGCM results are interpreted using previous results from horizontally homogeneous, two-layer, flat-bottom, f-plane, doubly periodic QG turbulence simulations and new results from two-layer β-plane QG turbulence simulations run in a basin geometry with both flat and rough bottoms. Baroclinicity in all of the simulations varies greatly with drag strength, with weak drag corresponding to more barotropic flow and strong drag corresponding to more baroclinic flow. The sensitivity of the baroclinicity in the QG basin simulations to bottom drag is considerably reduced, however, when rough topography is used in lieu of a flat bottom. Rough topography reduces the sensitivity of the eddy kinetic energy amplitude and horizontal length scales in the QG basin simulations to bottom drag to an even greater degree. The OGCM simulation behavior is qualitatively similar to that in the QG rough bottom basin simulations in that baroclinicity is more sensitive to bottom drag strength than are eddy amplitudes or horizontal length scales. Rough topography therefore appears to mediate the sensitivity of eddies in models to the strength of bottom drag. The sensitivity of eddies to parameterized topographic internal lee wave drag, which has recently been introduced into some OGCMs, is also briefly discussed. Wave drag acts like a strong bottom drag in that it increases the baroclinicity of the flow, without strongly affecting eddy horizontal length scales.

1. Introduction

This study focuses on the impact of frictional bottom boundary layer drag ("bottom drag" hereafter) on the statistics of the midocean eddy field, where eddies are defined as deviations from a time-mean. The focus on bottom drag is motivated by the substantial sensitivity of eddy statistics to bottom drag strength documented in numerous studies of flat-bottom quasi-geostrophic (QG) turbulence (*Salmon*, 1978, 1980; *Haidvogel and Held*, 1980; *Larichev and Held*, 1995; *Özgökmen and Chassignet*, 1998; *Riviere et al.*, 2004; *Arbic and Flierl*, 2004; *Thompson and Young*, 2006; *Arbic et al.*, 2007; *Arbic and Scott*, 2008; *Straub and Nadiga*, 2014). A consistent finding in such studies is that weak bottom drag leads to a vigorous inverse cascade yielding a strongly barotropic and energetic eddy field characterized by horizontal length scales significantly larger than the first baroclinic mode deformation radius (L_d). Computations of spectral kinetic energy fluxes made from satellite altimetry, idealized models, and realistic ocean general circulation model (OGCM) simulations (e.g., *Scott and Wang*, 2005; *Scott and Arbic*, 2007; *Schlösser and Eden*, 2007; *Qiu et al.*, 2008; *Tulloch et al.*, 2011; *Arbic et al.*, 2013, 2014; *Straub and Nadiga*, 2014) suggest that an inverse cascade to larger spatial scales is ubiquitous in the surface ocean. Indications are, however, that the inverse cascade proceeds over a relatively narrow range of oceanic length scales. Accordingly, observations demonstrate that the oceanic mesoscale eddy field lies far from the weak-drag limit of flat-bottom QG turbulence. For example, *Wunsch* (1997) finds that oceanic eddies are not strongly barotropic – instead, the kinetic energy levels in barotropic and first baroclinic modes are comparable. *Stammer* (1997) finds that length scales of ocean eddies are not much greater than L_d – instead, they are only slightly greater. *Arbic and Flierl* (2004) and *Arbic and Scott* (2008) argued that the "moderate" drag regime of QG turbulence (in between the weak drag and very strong drag limits) compared best to observations. However, it must be noted that most of the geostrophic tur-

bulence studies above are highly idealized, typically assuming not only QG dynamics, but in some cases also assuming horizontal homogeneity, zonal mean flows, a flat bottom, f-plane dynamics, and/or a severe truncation of vertical resolution to two layers. In some studies, the stratification is further simplified to consist of two layers of equal depths, thus precluding examination of the effects of surface-intensified stratification. The question therefore arises as to whether the sensitivities to bottom drag seen in the simple QG models used in many previous studies would also arise in more complex models such as high-resolution ocean general circulation models.

More realistic OGCMs have rough topography, non-zonal mean flows, the planetary β-effect, surface-intensified stratification, ageostrophic dynamics, many layers in the vertical direction (not just two), and stratification and mean flows that vary in the horizontal direction. Any one of these factors could alter the sensitivity of eddy statistics to bottom drag. For example, *Brüggemann and Eden* (2015) have demonstrated that the routes to energy dissipation associated with ageostrophic and quasi-geostrophic flows are qualitatively different, with the energy flux towards smaller scales in ($O(1)$ Rossby number) ageostrophic dynamics and towards larger scales in geostrophic turbulence. Increased vertical resolution implies that a lesser fraction of the water column will directly feel the effects of bottom drag, such that the sensitivity of eddy statistics to bottom drag is likely to be impacted. Horizontal inhomogeneities in more realistic models provide a more realistic environment for eddy evolution, and this may also affect eddy statistics (*Merryfield* 1998). *Venaille et al.* (2011) examined horizontally homogeneous QG turbulence simulations with a surface-intensified stratification, several layers in the vertical direction, imposed mean flows that project onto higher vertical modes, non-zonal mean flows, and the planetary β-effect. Similar to earlier studies, which often did not include many of these effects, they also found a strong sensitivity of the model eddy field to bottom drag strength (see their Table 2). Topographic effects, however, were not considered in their study, whereas it is well know that topography can profoundly influ-

ence the eddy field (*Rhines* 1970, 1977; *Treguier and Hua* 1988; *Treguier and McWilliams* 1990; *Dewar* 1998; *Sinha and Richards* 1999; *LaCasce and Brink* 2000; *Benilov et al.* 2004; *Hurlburt et al.* 2008; *Thompson* 2010; *Boland et al.* 2012; *Venaille* 2012; *Chen and Kamenkovich* 2013; *Abernathey and Cessi* 2014; *Stewart et al.* 2014; *Chen et al.* 2015). Some of these topographic effects involve small vertical length scales and are thus poorly represented in ocean general circulation models, which typically concentrate vertical resolution near the surface. One result of particular interest from the studies mentioned above is that topography can facilitate a downward transfer of energy (*Venaille* 2012). Note that at (forced-dissipated) statistical equilibrium, this need not imply a strong bottom intensification of kinetic energy because kinetic energy is continually input by the forcing and abyssal energy is removed by bottom friction.

Two additional factors typically absent in idealized studies, but that might also influence ocean eddy statistics, are internal lee waves and topographic blocking (together referred to as "wave drag" hereafter). Interest in wave drag, as a contributor to the oceanic energy budget and a potentially important addition to ocean model dynamics, has grown rapidly in recent years. The internal lee wave contribution to wave drag is the momentum flux due to wave generation over certain topographic length scales. The topographic blocking contribution to wave drag occurs when the streamline is parallel to the seafloor, and characterizes the hydraulic effects, low-level breaking, vortex shedding, flow separation, and low-level jets (*Baines*, 1995) that occur when flow impinges upon a topographic feature. Using a closure first developed by *Garner* (2005), *Trossman et al.* (2015) compared predictions of dissipation profiles in the Southern Ocean with microstructure profiler observations, and argued that the topographic blocking contribution to wave drag dominates the dissipation in the bottom 1000 meters. *Trossman et al.* (2013, 2016) found more than 0.4 TW of low-frequency mechanical energy dissipation associated with the combination of internal lee wave generation/breaking and topographic blocking in a model run with the *Garner* (2005)

wave drag parameterization. *Nikurashin and Ferrari* (2011), *Scott et al.* (2011), and *Wright et al.* (2014) all estimate that breaking internal lee waves dissipate at least 0.2 TW of low-frequency mechanical energy, comparable to the amount ($0.1 - 0.2$ TW) of dissipation estimated to occur via bottom drag (*Sen et al.* 2008; *Arbic et al.* 2009; *Trossman et al.* 2013; *Wright et al.* 2013; *Trossman et al.* 2016). Internal lee waves have also been found to be important in the momentum and vorticity budgets (*Naveira-Garabato et al.* 2013).

Wave drag parameterizes ageostrophic effects and can be thought of as distinct from form drag. The latter is a correlation between bottom pressure and topographic slope. It can be thought of in terms of geostrophic dynamics and is known to be particularly important in the Antarctic Circumpolar Current (ACC). Without form drag, closing the zonal momentum budget of the ACC involves either very large bottom drag or very large circumpolar transports (e.g., *Olbers et al.* (2004) and many others). In this context, recent work has explored the combined roles of bottom drag and topography in ACC settings. Various studies (*Hogg and Blundell* 2006; *Nadeau and Straub* 2012; *Nadeau and Ferrari* 2015) have shown circumpolar transport to increase with bottom drag. This can be easily understood in the strong drag limit of the quasi-geostrophic equations. In this limit, abyssal velocities are weak, so that the bottom layer streamfunction (equivalent to pressure in quasi-geostrophy) becomes near-constant. As such, form drag is diminished and circumpolar transport is increased. Primitive equation models also show transport to increase as bottom drag coefficients are made large, although it is likely that the degree to which circumpolar transport depends on the bottom drag may be related to the complexity of the bottom topography and may be less than implied by these idealized studies (e.g., *Nadeau et al.*, 2013; *Nadeau and Ferrari*, 2015).

In this study, we compare eddy statistics across realistic high-resolution OGCM simulations with varying strengths of bottom drag. For simplicity, the OGCM simulations analyzed here do

not include tides. In order to tease out the sensitivities very clearly, we vary the bottom drag coefficient C_d by a large factor (~ 500). Estimates of C_d values in the ocean vary by much less than that. Observations of boundary layer turbulence suggest C_d values of about 0.0025, with an uncertainty of a factor of about 3 in either direction (*Weatherly*, 1975; *Trowbridge et al.*, 1999; *Trowbridge and Elgar*, 2001; *Feddersen et al.*, 2003). We focus here on the statistics that *Arbic and Flierl* (2004) and *Arbic and Scott* (2008) focused upon – eddy baroclinicity or "vertical structure," eddy horizontal length scales, and eddy amplitudes – in their examination of the impact of bottom drag on two-layer flat-bottom QG turbulence. We compare the OGCM sensitivities to bottom drag with the sensitivities seen in previous studies of horizontally homogeneous, two-layer, flat-bottom, f-plane, doubly periodic QG turbulence, and the sensitivities seen in new two-layer, β-plane QG basin turbulence runs with both flat-bottom and rough-bottom conditions. Comparison of the multi-layer OGCM versus two-layer QG simulations may potentially shed light on the importance of ageostrophic effects and vertical resolution. Comparison of the horizontally homogeneous versus basin QG simulations may shed light on the importance of flow inhomogeneities. Comparison of the flat-bottom versus rough-bottom QG basin simulations illuminates the importance of rough bottom topography in setting the sensitivity of eddying flows to bottom drag strength. Motivated by the growing interest in wave drag, this paper will briefly discuss the impact of wave drag upon eddy statistics by examining the OGCM simulations run with wave drag in *Trossman et al.* (2013, 2016). We note that *Hurlburt and Hogan* (2008) also did simulations of an OGCM with varying values of bottom drag. They used an OGCM (the Naval Research Laboratory's Layered Ocean Model, NLOM) that is in a realistic domain, albeit with a number of simplifications relative to HYCOM. *Hurlburt and Hogan* (2008) focused on the response of western boundary current dynamics to bottom drag rather than on the impact of bottom drag on the inverse cascade of geostrophic turbulence.

The present paper is organized as follows. We first describe the high-resolution OGCM simulations, carried out in both Atlantic Ocean and global domains assuming different bottom drag parameter values, and in the global domain with and without wave drag. We then describe the β-plane QG basin simulations, carried out in a midlatitude double gyre setting —with and without rough topography and assuming different values for a bottom drag parameter. We also briefly discuss the setups for the *Arbic and Flierl* (2004) and *Arbic and Scott* (2008) two-layer, flat-bottom, horizontally homogeneous QG turbulence simulations that we will use here. We next describe various diagnostics used to measure the baroclinicity, amplitudes, and horizontal length scales of midocean eddies. Finally, we discuss the impact of bottom drag on eddy statistics in the QG and OGCM simulations, and the impact of wave drag on eddies in OGCM simulations. The diagnostics and results sections use some current meter observations and satellite altimeter products for comparison to the OGCM results. We end with some concluding remarks about the implications of this study.

2. Model configurations

The nominally $1/12^o$ and $1/25^o$ HYbrid Coordinate Ocean Model (HYCOM; *Bleck*, 2002; *Chassignet et al.*, 2003; *Halliwell*, 2004) simulations are on a tripole Mercator grid and have 32 hybrid layers in the vertical direction. HYCOM smoothly transitions between different vertical coordinates, depending on the relative strengths of the coordinates in different oceanic regimes (*Griffies et al.* 2000; *Chassignet et al.* 2006). The vertical coordinates are isopycnal in the subsurface open ocean, z-level in the open ocean mixed layer, and terrain-following in shallow regions. The performance of HYCOM without wave drag has been evaluated extensively in the North Atlantic (*Xu et al.*, 2016, and several references therein), in the North Pacific (*Kelly et al.* 2007), in the Indian Ocean (*Srinivasan et al.* 2009), and across the entire World Ocean (*Chassignet et al.*

2009; *Thoppil et al.* 2011). The performance of HYCOM with wave drag has been evaluated by *Trossman et al.* (2016) across the entire World Ocean.

We now discuss the vertical and horizontal eddy viscosity parameterizations in HYCOM. The K-Profile Parameterization (KPP; *Large et al.*, 1994) yields relatively strong vertical mixing in the mixed layer, with a smooth transition to weaker vertical mixing below. Background mixing is typically used in deep water with an assumed Prandtl number of three so that the vertical viscosity is a factor of three larger than the vertical diffusivity. Shear instability mixing is typically used in the mixed layer with an assumed Prandtl number of one. The horizontal viscosity includes the maximum of a *Smagorinsky* (1993) parameterization or Laplacian term with an additional biharmonic term (*Chassignet and Garraffo* 2001; *Chassignet and Marshall* 2008). Horizontal viscosity smooths out subgrid-scale noise. Here, "horizontal" means following a vertical coordinate layer.

For the global $1/25^o$ runs, we begin with a simulation that is spun-up using $1.125^o \times 1.125^o$ European Centre for Medium-Range Weather Forecasts (ECMWF) Re-Analysis (ERA-40) monthly mean forcing over 1978-2002 (*Kallberg et al.* 2004; *Uppala et al.* 2005), supplemented with higher frequencies. Six-hourly anomalies with respect to monthly means from the 2003 fields of the Navy Operational Global Atmospheric Prediction System (NOGAPS; *Rosmond et al.*, 2002) are added to the ERA-40 climatological wind forcing. The six-hourly winds are used during every model year in this way.

The global $1/25^o$ HYCOM simulation described above is first spun-up from rest for thirteen years using a value of the bottom drag coefficient ($C_d = 2.5 \times 10^{-3}$) that is designated as "mid" hereafter. The mid C_d value is the reference, or "control," value used in most HYCOM simulations. For legacy reasons, there is an assumed background tidal velocity (see, e.g., *Willebrand et al.*, 2001) of 5 cm s^{-1} for the first one and one-half years. The background tidal velocity is reduced to 2 cm s^{-1} for the next two and one-half years and 0 cm s^{-1} thereafter. Starting at the end of year 12,

this HYCOM simulation is further integrated in two different configurations. One configuration is run for an additional 5 years with $C_d = 2.5 \times 10^{-1}$ (designated "strong" hereafter). The other configuration is run for an additional 4 years with wave drag and the mid value of bottom drag (*Trossman et al.* 2013, 2016). Daily averages of vertical velocity profiles at select locations, daily averages of sea surface heights, and bi-monthly averages of all other diagnostic model output are saved during the final year (year 13 for the mid drag value, year 17 for the strong drag value, and year 16 for the wave drag simulation). Because all of the results in this paper are computed from years that are well beyond the years in which there is a legacy background tidal velocity, the legacy tidal velocity does not affect any of our conclusions here.

Only the $1/12^o$ Atlantic configuration is run with the weak value of the bottom drag coefficient ($C_d = 5.0 \times 10^{-4}$). The main reason for this is that simulations with the weak bottom drag coefficient require a very small baroclinic time step, making a global weak drag simulation prohibitively expensive. The $1/12^o$ Atlantic simulation is first spun-up from rest for twenty-three years with a mid bottom drag coefficient ($C_d = 2.5 \times 10^{-3}$). Sixteen spin-up years have a 5 cm s^{-1} background tidal velocity and another seven years have no background tidal velocity. This simulation is then integrated for an additional 4 years with the weak value of the bottom drag ($C_d = 5.0 \times 10^{-4}$). Daily averages of vertical velocity profiles at select locations, daily averages of sea surface heights, and monthly averages of all other diagnostic model output are saved during the final year (year 23 for the mid drag simulation and year 27 for the weak drag simulation). Table 1 presents the C_d values as well as the barotropic and baroclinic time steps of the HYCOM simulations analyzed in this paper. Note that both the weak and strong bottom drag runs require much smaller baroclinic time steps than the mid strength bottom drag (or control) runs. The wave drag simulation also requires a smaller time step.

The flat bottom QG β-plane basin model configuration used here is taken directly from *Straub and Nadiga* (2014). It has a uniform horizontal grid with $\Delta x \approx 7.8$ km, or about four grid points per deformation radius, L_d, here taken to be 30 km. The number of grid points is 512×512. The upper and lower layer thicknesses are set to be 1000 and 3000 meters, respectively. A double gyre (i.e., sinusoidal) zonal wind-stress forcing is applied to the upper layer potential vorticity equation. Biharmonic friction is added to damp enstrophy. A version of free slip conditions appropriate for biharmonic dissipation is applied; specifically, both vorticity and its Laplacian are set to zero at the horizontal boundaries. A Rayleigh (linear Stommel bottom) drag is applied to the lower layer only. The QG basin simulations analyzed here differ only in their bottom drag coefficient ($r_{QG} = 8.0 \times 10^{-10}$ s^{-1}, $r_{QG} = 8.0 \times 10^{-8}$ s^{-1}, and $r_{QG} = 8.0 \times 10^{-6}$ s^{-1} are used, with the middle value taken as the nominal value) and in their bottom boundary condition (flat bottom and rough bottom topography). The rough topography used is taken from the North Atlantic region of the *Smith and Sandwell* (1997) bathymetric product. We want a topography that is rough, but is not rough at the model grid scale, as the latter would lead to numerical noise. In order to achieve this, we perform a two-dimensional interpolation of the *Smith and Sandwell* (1997) topography to a uniform 128×128 grid in the region bounded by $18.0 - 54.1^o$W, $7.3 - 43.4^o$N, and then perform another interpolation to the model's 512×512 grid within the same domain. The bathymetry used in our rough bottom QG simulations is shown in Fig. 1. The figure shows the Mid-Atlantic Ridge cutting through the domain from the upper-right towards the lower-left corners. Note that our topography violates the QG assumption that the bottom layer depth variations are much less than the total depth. We also note that, as in most QG double gyre simulations, the formal requirements that $\beta L/f_0$ and ζ/f_0 be small are also violated, for linear meridional gradient in the Coriolis parameter β, topographic horizontal length scale L, Coriolis parameter f_0, and relative vorticity ζ. The time-averaged total energies are saved for each of the six QG basin model configurations,

following an initial spin-up sufficient to allow for energy levels to equilibrate. Daily output is saved for the ensuing final 135 days beyond the initial spin-up.

The horizontally homogeneous, two-layer, flat-bottom, f-plane, doubly periodic QG results are taken from *Arbic and Flierl* (2004) and *Arbic and Scott* (2008). A linear bottom drag was used in the former paper while a quadratic bottom drag was employed alongside a linear drag in the latter paper. *Arbic and Scott* (2008) demonstrated that the impacts of bottom drag strength on the vertical structure, amplitude, and horizontal length scales of eddy kinetic energy are qualitatively similar whether linear or quadratic bottom drag is used; however, the sensitivity to drag is reduced when the drag is quadratic. The horizontally homogeneous QG results are run in a doubly periodic domain, with an imposed, baroclinically unstable mean flow meant to mimic the flows in a mid-ocean gyre. Equilibration results when the energy extracted by eddies from the mean flow is balanced by the energy dissipated by bottom drag.

3. Diagnostics and observations

For the most part, we compare our various model simulations with each other. However, we will also compare the sea surface height (SSH) variance, the geostrophic surface kinetic energy (SKE), and the vertical structure of the kinetic energy (KE) of the OGCM simulations with observations. The "observed" geostrophic SKE and SSH variance are taken from satellite altimetry products. To make the observations comparable with our model output, a mean SSH product (*Andersen and Knudsen* 2009; *Andersen* 2010) is added to the SSH anomalies from satellite altimetry before computing the observed geostrophic SKE and SSH variance. Geostrophic SKE is computed from the SSHs using a nine-point stencil according to the method outlined in *Arbic et al.* (2012). The model's SSH variance and geostrophic SKE are calculated from daily averaged model output.

KE profiles at current meter locations (taken from the Global Multi-Archive Current Meter Database)[1] will be compared to the output of our global HYCOM simulations. The current meter velocities were filtered using a Butterworth filter with half-power of 3 and a daily cutoff period to eliminate tides and other higher frequency motions that are not present in the daily-averaged model output. We show the average vertical profile of the KE computed over the locations where current meter observations of at least a month duration exist. We place the KE at each horizontal location into 500 meter depth bins in the upper 4000 meters because 500 meters is a typical vertical resolution of abyssal layers in HYCOM; the vertical spacing between current meters on a typical mooring is of the same order of magnitude.

We measure the vertical structure, or baroclinicity, of eddy KE in two ways: as the ratio of the baroclinic to barotropic KE (KE_{BC} to KE_{BT}) and as the ratio of near-surface to near-bottom KE. Here, KE_{BT} is the kinetic energy of the depth-averaged flow, and KE_{BC} is the kinetic energy of the deviations from the depth-averaged flow. For QG,

$$\psi_{BT} = \frac{H_1\psi_1 + H_2\psi_2}{H_1 + H_2} \tag{1}$$

$$\psi_{BC} = \sqrt{H_1 H_2}\frac{\psi_1 - \psi_2}{H_1 + H_2},$$

where H_1 and ψ_1 are the layer thickness and streamfunction in the upper layer, and H_2 and ψ_2 are the layer thickness and streamfunction in the bottom layer. *Arbic and Flierl* (2004) found the KE_{BC} to KE_{BT} ratio to be a more useful diagnostic for quantifying baroclinicity in weak bottom drag QG turbulence simulations, while the surface-to-bottom KE ratio was more useful in the strong drag limit. Only in our Atlantic simulations do we quantify baroclinicity using KE_{BC}/KE_{BT}. In both our Atlantic and global simulations, we use the top 100 meters and bottom 500 meters to represent the near-surface and near-bottom ocean; we will refer to the ratio of the two as KE_{top100}/KE_{bot500}.

[1]See: http://stockage.univ-brest.fr/˜scott/GMACMD/updates.html (*Scott et al.* 2010). These observations were quality controlled by *Timko et al.* (2013) for effects such as blow-over.

This choice is made because the surface mixed layer is typically on the order of 100 meters thick, while the bottom two layers together in HYCOM are typically about 500 meters thick. When calculating the ratios, we omit all grid points where the water is shallower than 500 meters. When tabulating the area-averaged KE_{BC}/KE_{BT} and KE_{top100}/KE_{bot500} ratios, we also omit all grid points within 30 indices of the coasts because in such locations there can be infinitesimal layer thicknesses that lead to finite transports but very large values of KE.

Eddy horizontal length scale diagnostics are also computed. As in the doubly periodic QG turbulence simulations of *Arbic and Flierl* (2004) and *Arbic and Scott* (2008), we examine the length scales L_{KE} of eddy SKE and L_{BT} of eddy barotropic KE. The HYCOM eddy SKE length scales are computed assuming a geostrophic streamfunction, $\psi = g\eta/f$, where η is the daily-averaged SSH, $g = 9.806$ m s^{-2} is the acceleration due to gravity, and f is the Coriolis parameter. The SKE length scale is

$$L_{KE} \doteq \left[\frac{\int \kappa E_{KE}(\kappa) d\kappa}{\int E_{KE}(\kappa) d\kappa} \right]^{-1}, \tag{2}$$

where κ is the isotropic horizontal wavenumber and $E_{KE}(\kappa) = \kappa^2 |\hat{\psi}|^2$ is the geostrophic SKE spectrum, where $\hat{}$ denotes a Fourier transform. The QG model's eddy SKE length scales are computed from the upper layer's streamfunction. The QG model's eddy length scales associated with KE_{BT} are calculated similarly, but using $E_{BT} = |\hat{u}_{BT}|^2 + |\hat{v}_{BT}|^2$ in place of E_{KE}. Because it suffices to show the HYCOM KE_{BT} fields for the conclusions we draw about L_{BT}, HYCOM L_{BT} are not calculated. The two-dimensional Fourier transforms above are calculated using data from $20^o \times 20^o$ regions. Using output from our HYCOM simulations, ψ is interpolated onto a uniformly spaced (≈ 7.8 km) latitude-longitude grid. The temporal mean and spatial trends within each box were removed for the HYCOM simulations. For the QG basin simulations, the temporal mean trend within each box was removed; no interpolation was necessary since these data were output on a uniformly spaced grid.

Because of their relevance to interpreting the differences between the simulations with varied bottom drag strengths and the simulations with wave drag, we describe the bottom drag and wave drag contributions to the KE equation. This KE equation can be written as in *Trossman et al.* (2013)

$$P_{KE,t} + P_{KE,adv} = P_{press} + P_{input} - P_{output} + C_{KE\rightarrow PE} \tag{3}$$

Here, $P_{KE,t}$ is the time derivative of the globally integrated KE, $P_{KE,adv}$ is the KE change due to advective fluxes across the sea surface, P_{press} is the divergence of KE associated with pressure differentials at the sea surface, P_{input} is the wind energy input, P_{output} is the sum of all dissipative terms such as bottom drag and wave drag (see below), and $C_{KE\rightarrow PE}$ is the conversion rate of KE to PE. Because of the form of the wave drag parameterization in the momentum equations (*Trossman et al.* 2013, 2016), it can be thought of as a linear bottom boundary layer drag with a spatially varying coefficient (r_{drag}). The energy dissipation rate due to quadratic bottom boundary drag is given by *Taylor* (1919)

$$D_{BD} = \rho_0 C_d |\mathbf{u}_b|^3. \tag{4}$$

The energy dissipation due to a combination of topographic blocking and internal lee wave drag is given by *Trossman et al.* (2013)

$$D_{WD} = \rho_0 r_{drag} |\mathbf{u}_d|^2. \tag{5}$$

Here, $\rho_0 = 1035$ kg m^{-3} is the average density of seawater with respect to 2000 dbar; C_d is the quadratic drag coefficient; $\mathbf{u}_b$ is the velocity averaged over the bottom H_{BD} meters and $\mathbf{u}_d$ is the velocity averaged over the bottom H_{WD} meters, with $|\cdot|$ indicating a magnitude; r_{drag} is a positive-definite decay rate times a vertical length scale, computed from $\mathbf{u}_d$ and a power spectrum associated with the underlying topography; $H_{BD} = 10$ meters is the height range above the seafloor (up to the surface if shallower than 10 meters) over which quadratic bottom drag is applied in the

model; and $H_{WD} = 500$ meters is the height range above the seafloor (up to the surface if shallower than 500 meters) over which wave drag is applied in the model.

4. Results

Using horizontal eddy length scales, KE budget terms, geostrophic SKE, SSH variances, and ratios of KE_{BC} to KE_{BT} and near-surface to near-bottom KE, we will evaluate the impact of bottom drag strength on HYCOM and QG β-plane basin dynamics. We compare sensitivities in our HYCOM and QG basin simulations with results based on simpler two-layer, flat bottom, horizontally homogeneous QG turbulence studies. We also compare the SSH variance, geostrophic SKE, and vertical structure of KE from our HYCOM simulations with observations to assess the degree to which the bottom drag strength (C_d) is important in maintaining realistic eddy statistics in these simulations. We finish this section by examining how eddy statistics are altered upon addition of wave drag, using the metrics described above.

a. SSH variance and geostrophic SKE

The area-averaged geostrophic SKE in the HYCOM simulations, which have realistic bathymetry, is relatively insensitive to bottom drag strength, being only slightly increased with larger bottom drag strength and slightly decreased with smaller bottom drag strength (Figs. 2a-d; Table 2). This contrasts with previous studies of two-layer flat-bottom doubly periodic QG turbulence simulations (e.g., *Arbic and Flierl* 2004; *Arbic and Scott* 2008) for which the sensitivity is much greater.[2]

SSH variance shows a somewhat larger sensitivity (Fig. 3; Table 2). For example, the strong bottom drag simulation shows greater SSH variance in the Gulf Stream Extension than is the case

[2]The geostrophic SKE is larger in each of the HYCOM model simulations than in AVISO (Fig. 2e). This is due to a known deficiency of energy in the AVISO product (e.g., *Chelton et al.*, 2011).

for the control run (Figs. 3a and 3c). This is also true in the intensified jet regions outside that of the Gulf Stream as well. Conversely, the weak bottom drag run shows less SSH variance in energetic currents (Figs. 3b and 3d).

We infer that the changes in SSH variances shown in Fig. 3 are due to increased near-surface eddy-driven mixing in the strong bottom drag simulations. *Radko et al.* (2014) postulates that eddy-driven mixing increases with shear, and we find evidence that the near-surface shear increases with drag coefficient (see the discussion of Fig. 4 below). Furthermore, the ageostrophic flow is affected through the curl of the wind stress, mostly in regions with intensified jets (not shown). We surmise that there are alterations in baroclinic instability due to differences in an inferred conversion rate between kinetic and potential energy change with varied bottom drag strength. *Trossman et al.* (2013, 2016) argued, making reference to (3), that the conversion rate between kinetic and potential energy must change when wave drag is included and the same energetics argument holds for our experiment with increased bottom drag strength.

b. Vertical structure of the kinetic energy

The vertical structure of KE in our strongly damped HYCOM simulations is qualitatively consistent with that seen in idealized QG turbulence simulations, but agrees poorly with observations. Table 3 demonstrates that the ratio of KE in the upper to lower layers is greatly increased in the strong drag HYCOM experiment, as would be anticipated from strong drag horizontally homogeneous QG turbulence results (*Arbic and Flierl* 2004; *Arbic and Scott* 2008). Fig. 4b shows KE profiles for the low-passed observations and the global $1/25^o$ strong- and mid-strength bottom drag simulations. Data are temporally averaged at each location in the Global Multi-Archive Current Meter Database and then averaged over all locations shown in Fig. 4a. Strong bottom drag renders a more baroclinic, surface-intensified flow. The KE from the strong drag simulation

(red curve in Fig. 4b) is greatly reduced near the seafloor and less so at shallower depths. The poor comparison between the strong-drag run and observations suggests that the real ocean is not in a strong-drag regime, consistent with the conclusions of *Arbic and Flierl* (2004) and *Arbic and Scott* (2008). Baroclinicity in the weak- versus mid-drag HYCOM simulations also behaves in a qualitatively similar way to what is observed in horizontally homogeneous QG turbulence (*Arbic and Flierl* 2004; *Arbic and Scott* 2008). Table 3 suggests that the Atlantic weak-drag simulation is more barotropic (less surface-intensified) than the mid-drag simulation.

We next consider geographical distributions of baroclinicity. Figure 5 shows maps of KE_{top100}/KE_{bot500} for the global mid- and strong-drag HYCOM simulations and Fig. 6 shows maps of the same quantity for the Atlantic mid- and weak-drag HYCOM simulations[3]). The locations where KE shows strong baroclinicity in the global maps of Fig. 5 tend to be within 40^o of the equator or confined within bands in the Southern Ocean. Fig. 5 indicates that the number of grid points that are highly baroclinic is greater in the strong-drag simulation than in the mid-drag simulation, consistent with expectations from horizontally homogeneous QG turbulence simulations. In the weak drag simulations, baroclinicity is considerably reduced (compare Figs. 6a and 6b). Overall, baroclinicity of the KE in HYCOM behaves qualitatively as one might expect from from idealized, flat-bottom, horizontally homogeneous QG turbulence simulations: the flow becomes distinctly more barotropic with weak drag and more baroclinic with strong drag. An important difference from this classical picture is that surface and barotropic KE are individually less sensitive than is the case in classic studies of QG turbulence. This can be seen by inspection of Fig. 7, which displays KE_{BT} in the North Atlantic for the global and Atlantic HYCOM simulations with

[3]We did not save the total or baroclinic component of the KE for the $1/25^o$ global simulations due to the large hard disk space requirements needed to save these fields. The combination of Figs. 4b and 5 with Table 3 are sufficient to demonstrate that the flow becomes more baroclinic with stronger bottom drag.

varying bottom drag strength. Although KE_{BT} is weaker when bottom drag is stronger (Fig. 7), this dependence is much less pronounced than is the signal as seen in baroclinicity (Figs. 5 and 6).

Our QG basin simulations allow us to examine the impacts of rough topography and lateral inhomogeneities on eddy statistics in QG flow. Fig. 8 displays the baroclinicity (quantified with both of the measures discussed earlier), as well as the surface and barotropic eddy horizontal length scales, in the QG basin simulations (with both rough and flat bottom topography), the previously reported horizontally homogeneous, two-layer, flat-bottom, f-plane, doubly periodic QG simulations of *Arbic and Flierl* (2004) and *Arbic and Scott* (2008), and the OGCM simulations. The abscissa of Fig. 8 represents the nondimensional friction strength, as defined by *Arbic and Scott* (2008) for the doubly periodic simulations, and defined by the ratio of the friction value to the nominal, or "control" value, for the QG basin and OGCM simulations. The QG basin simulations show that increased bottom drag leads to a more baroclinic flow, as expected (see blue curves in Figs. 8a-b), and in qualitative consistency with the QG turbulence results shown in Figs. 8a-b (black curves). Also as expected, overall there is less KE in the QG basin simulations when bottom drag strength is increased (Table 4).[4] However, the sensitivity of baroclinicity and eddy energy to bottom drag strength is greatly reduced from what is seen in the horizontally homogeneous QG turbulence results, especially when rough topography is introduced into the QG basin simulations (e.g., compare the squares-solid blue curve to the diamonds-dot-dashed blue curve relative to the black curves in Figs. 8a-b, and the much greater sensitivity in Table 4 for the flat versus rough bottom simulations). This reduced sensitivity relative to horizontally homogeneous QG turbulence results is also seen in the HYCOM simulations over areas of rough topography, e.g., over a sub-domain of the North Atlantic (between $59.3^o - 39.3^o$W and $19.6^o - 39.6^o$N) close to the one

[4]The eddy kinetic energy is only at a level near that of observations when the bottom drag coefficient lies in a particular range, but this range is considerably broader when rough topography is present than when a flat bottom is employed.

shown in Fig. 1 (red curves in Figs. 8a-b). It seems clear that rough topography accounts for much of the discrepancy between our HYCOM simulations and expectations from classic studies of flat-bottom QG turbulence.

c. Surface eddy horizontal length scales

We next consider eddy horizontal length scales. In our HYCOM simulations, length scales L_{KE} associated with SKE are fairly insensitive to bottom drag strength (Fig. 8d; Table 5). Although we did not explicitly calculate a length scale for the KE in the barotropic mode of our HYCOM simulations, visual inspection of Fig. 7 suggests that it too is relatively insensitive to bottom drag strength. In contrast, the surface eddy horizontal length scales increase more dramatically with reducing drag strength in the weak-drag limit of the horizontally homogeneous, two-layer, flat-bottom, f-plane, doubly periodic QG turbulence results of *Arbic and Flierl* (2004) and *Arbic and Scott* (2008), as can be seen in Fig. 8d. The increase in surface length scales in these previous simulations is mainly due to an increase in the barotropic length scale (Fig. 8c).

To investigate a possible reason for the weak sensitivity of HYCOM eddy horizontal length scales to bottom drag relative to flat-bottom, horizontally homogeneous QG turbulence results, we compare eddy length scales from our QG basin simulations with and without rough topography. We consider eddy length scales associated with barotropic KE (Fig. 8c) and surface, or upper layer, KE (Fig. 8d). As with the HYCOM simulations (red curves in Figs. 8d), there is no general trend for the eddy length scales as a function of bottom drag strength in our rough bottom QG basin simulations. However, the eddy length scales in the flat-bottom QG basin simulations behave more like the previous flat-bottom doubly periodic QG turbulence results – both barotropic and surface eddy length scales increase greatly as drag is weakened in the weak drag limit. Overall, our results suggest that rough topography reduces the sensitivity of eddy horizontal length scales to bottom

drag. This insensitivity can be visualized through examination of snapshots of the upper layer streamfunction, shown in Fig. 9, for the QG basin simulations. The flat bottom simulations show large qualitative differences as drag strength is altered. With rough topography, this sensitivity is markedly reduced. In addition, we note that the presence of topography matters less to the surface streamfunction when the drag is strong. For instance, the streamfunctions for the simulations with strong-drag in flat- and rough-bottom configurations (Figs. 9c and 9f, respectively) are more similar to each other than are the streamfunctions for the simulations with mid- or weak-drag in flat- and rough-bottom configurations (Figs. 9a,d and 9b,e). This is because the bottom horizontal flow, $\vec{u}$, approaches zero in the strong-drag regime, and the impact of topography on QG flows is proportional to $\vec{u} \cdot \nabla h$, where h is the bottom topography. Our QG basin simulation results are consistent with the finding from previous studies (e.g., *Nadeau et al.*, 2013) that use of realistic rough topography increases baroclinicity (e.g., compare upper and lower layer kinetic energies in their Table 2).

It seems clear that rough topography acts to reduce the sensitivity of eddy horizontal length scales to bottom drag strength. Other differences between our HYCOM simulations and many classic studies of QG turbulence include vertical resolution (e.g., the number of layers, which is often only two in QG turbulence models); horizontal inhomogeneities; and other modeling choices, such as the choice of linear versus quadratic parameterizations of bottom drag. Although it is difficult to make a direct comparison, the use of a quadratic bottom drag instead of a linear drag may also account for part of the weakened sensitivity in HYCOM. *Arbic and Scott* (2008) showed that the sensitivities in QG turbulence to linear drag are greater than those for quadratic drag, as can be seen in Fig. 8 here. It seems unlikely that the reduced sensitivity seen in our HYCOM simulations (relative to classic studies) is strongly affected by vertical resolution, ageostrophic dynamics, or horizontal inhomogeneity. In support of this statement, we note that *Hurlburt et al.*

(2008) used a realistic OGCM similar to HYCOM, but with a flat bottom. They find much larger changes in mean SSH in response to changes in bottom drag than we see, despite the inclusion of horizontal inhomogeneity, ageostrophic dynamics, and higher vertical resolution in their model.

A working hypothesis for why rough topography acts to reduce the sensitivity of eddy horizontal length scales to bottom drag is that barotropization of baroclinic energy gets short-circuited in the presence of rough bottom topography. Barotropization of baroclinic energy extracts baroclinic energy from scales near the deformation radius and injects it into the barotropic mode, typically at somewhat larger horizontal scales. This energy remains resident in the barotropic mode, essentially until it is removed by bottom friction. With rough topography, much of this barotropic energy can be transferred back to the baroclinic mode; that is, interaction between topography and the barotropic streamfunction forces the baroclinic mode. Assuming this to occur at a comparable or faster rate than the rate at which bottom drag acts to remove barotropic energy, the barotropization process becomes effectively "short-circuited". Our hypothesis and those posed by previous studies (e.g., *Hurlburt et al.*, 2008) on the influence of rough topography on eddying flows would explain the relatively small changes observed in geostrophic SKE, SSH variance, and eddy horizontal length scales here.

d. Effect of wave drag

The strong and weak values of bottom drag used here help to demonstrate the impact of bottom drag strength on eddy statistics, but these extreme drag values lie outside of physically plausible limits. Aside from the "mid" value of $C_d = 2.5 \times 10^{-3}$, an additional plausible momentum sink in the ocean is that associated with wave drag, as described in *Trossman et al.* (2013, 2016). Here, we briefly investigate whether the sensitivity of eddy statistics to the presence of a physically plausible

wave drag momentum sink is qualitatively similar to the sensitivity seen with the extremes of bottom drag strength discussed in previous sections.

Including wave drag and boosting bottom drag strength impact HYCOM in a qualitatively similar manner. The near-bottom flows are also weakened in the HYCOM simulation with wave drag such that the vertical profile of KE is more baroclinic relative to the simulation without wave drag (Fig. 10; Table 3; *Trossman et al.*, 2016 - their Figs. 11a-d). As with the sensitivity of HYCOM eddy length scales to bottom drag strength (Fig. 8d; Table 5), L_{KE} in HYCOM is fairly insensitive to the presence of wave drag (Table 5). Area-averaged SSH variance and geostrophic SKE in HYCOM are both sensitive at the $\sim$20% level to the inclusion of wave drag (*Trossman et al.*, 2016 - their Figs. 5 and 7; their Table 2; also see Table 2 in this paper). Lastly, the conversion rate between kinetic and potential energy must change with the same sign when wave drag is included as when bottom drag strength is increased.

The responses of the HYCOM simulations with wave drag and strong bottom drag, however, are not identical. When wave drag is included, the SSH variance and geostrophic SKE are actually decreased, in contrast to the slight increases seen with increasing bottom drag (Table 2). This demonstrates the fundamentally different physical consequences of including wave drag relative to boosting bottom drag. Here we surmise that the spatially varying coefficient, r_{drag}, in the wave drag parameterization is the source of the qualitatively different responses of SSH variance and geostrophic SKE to the presence of wave drag as opposed to increasing bottom drag strength. From the results of *Hurlburt and Hogan* (2008), who varied bottom drag strength using only six layers in the vertical direction and a flat bottom in a model very similar to HYCOM, we suggest that applying a bottom drag over a much larger bottom layer thickness than in our HYCOM simulations would not cause qualitatively different behavior in the geostrophic SKE and SSH variance. We also suggest, based upon the horizontally homogeneous QG turbulence results of *Arbic and Scott*

(2008), that using a linear, as opposed to quadratic, bottom drag near the seafloor is not the cause of the qualitatively different behaviors seen when using wave drag versus bottom drag.

5. Conclusions

The present study investigates the sensitivity of midocean eddy statistics to bottom drag, rough topography, and wave drag in models of varying complexity. A primary focus is on whether the conclusions drawn from horizontally homogeneous, two-layer, flat-bottom, f-plane, doubly periodic QG turbulence simulations about sensitivity to bottom drag (e.g., *Arbic and Flierl*, 2004; *Arbic and Scott*, 2008) qualitatively apply to more realistic ocean models. In the QG basin and realistic OGCM simulations with strong bottom drag studied here, the KE is reduced in the bottom-most layer and generally becomes more baroclinic, as in the earlier two-layer doubly periodic QG results. As a result, the agreement with the vertical structure, or baroclinicity, of eddy KE in current meter observations is better for the OGCM simulations with a nominal "mid" value of bottom drag than for the OGCM simulations with a strong bottom drag. In the QG basin and OGCM simulations with weak bottom drag studied here, the KE becomes more barotropic, again in accordance with earlier two-layer doubly periodic QG results. However, the sensitivity of the baroclinicities in the QG basin simulations to bottom drag is reduced for rough bottom conditions relative to flat bottom conditions, suggesting that rough topography mediates the sensitivity of baroclinicity to bottom drag.

The qualitative results about the horizontal eddy length scales seen in horizontally homogeneous, two-layer, flat-bottom, f-plane, doubly periodic QG turbulence damped by very weak or strong bottom drag are not seen in the QG basin simulations performed here with rough topography. In line with earlier results (e.g., *Treguier and Hua*, 1988), the use of rough topography reduces the sensitivity of eddy horizontal length scales to bottom drag strength in QG basin simulations.

Our QG basin simulations suggest that the bathymetry of the more realistic OGCM simulations is partially responsible for the relatively weak impact of bottom drag or wave drag on horizontal eddy length scales.

Acknowledgments. The authors would like to thank the two anonymous reviewers for comments that helped us to improve manuscript, and Michael Messina for his computer support. D. S. Trossman and B. K. Arbic gratefully acknowledge support from National Science Foundation (NSF) grant OCE-0960820 and Office of Naval Research (ONR) grants N00014-11-1-0487 and N00014-15-1-2288. Grants of computer time were provided by the Department of Defense (DoD) High Performance Computing Modernization Program and by the National Center for Atmospheric Research (NCAR) Yellowstone university allocations. We would like to acknowledge high-performance computing support from Yellowstone (ark:/85065/d7wd3xhc) provided by NCAR's Computational and Information Systems Laboratory, sponsored by the National Science Foundation. We would also like to acknowledge high-performance computing support from the U.S. Army Engineer Research and Development Center DoD Supercomputing Resource Center in Vicksburg, MS. The output files for the HYCOM model runs analyzed in this paper are archived at the Department of the Navy Shared Resource Center (DSRC) at the Stennis Space Center. The files stored there can be accessed after obtaining an account at the facility. The output files for the QG model runs analyzed in this paper are archived on a local University of Michigan machine and are available upon request. This is NRL contribution NRL/JA/7320-16-3270 and has been approved for public release.

References

Abernathey, R., and P. Cessi, 2014: Topographic enhancement of eddy efficiency in baroclinic equilibration. *J. Phys. Oceanogr.*, **44**, 2107–2126.

Andersen, O. B., and P. Knudsen, 2009: The DNSC08 mean sea surface and mean dynamic topography, *J. Geophys. Res.-Oceans*, **114**, C11, doi:10.1029/2008JC005179.

Andersen, O. B., 2010: The DTU10 Gravity field and Mean sea surface, Second international symposium of the gravity field of the Earth (IGFS2), Fairbanks, Alaska.

Arbic, B. K., and G. R. Flierl, 2004: Baroclinically unstable geostrophic turbulence in the limits of strong and weak bottom Ekman friction: application to midocean eddies. *J. Phys. Oceanogr.*, **34**, 2257–2273.

Arbic, B. K., G. R. Flierl, and R. B. Scott, 2007: Cascade inequalities for forced-dissipated geostrophic turbulence. *J. Phys. Oceanogr.*, **37**, 1470–1487.

Arbic, B. K., and R. B. Scott, 2008: On quadratic bottom drag, geostrophic turbulence, and oceanic mesoscale eddies. *J. Phys. Oceanogr.*, **38**, 84–103.

Arbic, B. K., J. F. Shriver, P. J. Hogan, H. E. Hurlburt, J. L. McClean, E. J. Metzger, R. B. Scott, A. Sen, O. M. Smedstad, and A. J. Wallcraft, 2009: Estimates of bottom flows and bottom boundary layer dissipation of the oceanic general circulation from global high-resolution models. *J. Geophys. Res.*, **114**, C02024.

Arbic, B. K., R. B. Scott, D. B. Chelton, J. G. Richman, and J. F. Shriver, 2012: Effects of stencil width on surface ocean geostrophic velocity and vorticity estimation from gridded satellite altimeter data. *J. Geophys. Res.-Oceans*, **117**, C03029.

Arbic, B. K., K. L. Polzin, R. B. Scott, J. G. Richman, and J. F. Shriver, 2013: On eddy viscosity, energy cascades, and the horizontal resolution of gridded satellite altimeter products. *J. Phys. Oceanogr.*, **43**, 283–300.

Arbic, B. K., M. Müller, J. G. Richman, J. F. Shriver, A. J. Morten, R. B. Scott, G. Sérazin, and T. Penduff, 2014: Geostrophic turbulence in the frequency-wavenumber domain: eddy-driven low-frequency variability. *J. Phys. Oceanogr.*, **44**, 2050–2069.

Baines, P. G., 1995: Topographic effects in stratified flows. *Cambridge Univ. Press*, Cambridge, U. K.

Benilov, E. S., J. Nycander, and D. G. Dritschel, 2004: Destabilization of barotropic flows by small-scale topography. *J. Fluid. Mech.*, **517**, 359–374.

Bleck, R., 2002: An oceanic general circulation model framed in hybrid isopycnic-Cartesian coordinates. *Ocean Modelling*, **37**, 55–88.

Boland, E. J. D., A. F. Thompson, E. Shuckburgh, and P. H. Haynes, 2012: The formation of nonzonal jets over sloped topography. *J. Phys. Oceanogr.*, **42**, 1635–1651.

Brüggemann, N., and C. Eden, 2015: Routes to dissipation under different dynamical conditions. *J. Phys. Oceanogr.*, **45**, 2149–2168.

Chassignet, E. P., and Z. D. Garraffo, 2001: Viscosity parameterization and the Gulf Stream separation. In "From Stirring to Mixing in a Stratified Ocean". *Proceedings of the 12th 'Aha Huliko'a Hawaiian Winter Workshop*. U. of Hawaii. P. Muller and D. Henderson, Eds., 37–41.

Chassignet, E. P., L. T. Smith, G. R. Halliwell, and R. Bleck, 2003: North Atlantic simulations with the Hybrid Coordinate Ocean Model (HYCOM): impact of the vertical coordinate choice, reference pressure, and thermobaricity. *J. Phys. Oceanogr.*, **33**, 2504–2526.

Chassignet, E. P., H. E. Hurlburt, O. M. Smedstad, G. R. Halliwell, A. J. Wallcraft, E. J. Metzger, B. O. Blanton, C. Lozano, D. B. Rao, P. J. Hogan, and A. Srinivasan, 2006: Generalized vertical coordinates for eddy-resolving global and coastal ocean forecasts. *Oceanography*, **19**(1), 20–31.

Chassignet, E. P., and D. P. Marshall, 2008: Gulf Stream separation in numerical ocean models. In "Eddy-Resolving Ocean Modeling", M. Hecht and H. Hasumi, Eds., *AGU Monograph Series*, 39–62.

Chassignet, E. P., H. E. Hurlburt, E. J. Metzger, O. M. Smedstad, J. A. Cummings, G. R. Halliwell, R. Bleck, R. Baraille, A. J. Wallcraft, C. Lozano, H. L. Tolman, A. Srinivasan, S. Hankin, P. Cornillon, R. Wesberg, A. Barth, R. He, F. Werner, and J. Wilkin, 2009: US GODAE global ocean prediction with the HYbrid Coordinate Ocean Model (HYCOM). *Oceanography*, **22**, (2, Sp. Iss. SI), 64–75.

Chelton, D. B., M. G. Schlax, and R. M. Samelson, 2011: Global observations of nonlinear mesoscale eddies. *Prog. Oceanogr.*, **91**, 167–216.

Chen, C., and I. Kamenkovich, 2013: Effects of topography on baroclinic instability. *J. Phys. Oceanogr.*, **43**, 790–804.

Chen, C., I. Kamenkovitch, and P. Berloff, 2015: On the dynamics of flows induced by topographic ridges. *J. Phys. Oceanogr.*, **45**, 927–940.

Dewar, W., 1998: Topography and barotropic transport control by bottom friction. *J. Mar. Res.*, **56**, 295–328

Feddersen, F., E. L. Gallagher, R. T. Guza, and S. Elgar, 2003: The drag coefficient, bottom roughness, and wave-breaking in the nearshore. *Coast. Engin.*, **48**, 189–195.

Garner, S. T., 2005: A topographic drag closure built on an analytical base flux, *J. Atmos. Sci.*, **62**, 2302–2315.

Griffies, S. M., C. Böning, F. O. Bryan, E. P. Chassignet, R. Gerdes, H. Hasumi, A. Hirst, A.-M. Treguier, and D. Webb, 2000: Developments in ocean climate modelling. *Ocean Modelling*, **2**, 123–192.

Haidvogel, D. B., and I. M. Held, 1980: Homogeneous quasigeostrophic turbulence driven by a uniform temperature gradient. *J. Atmos. Sci.*, **37**, 2644–2660.

Halliwell, G. R., 2004: Evaluation of vertical coordinate and vertical mixing algorithms in the HYbrid-Coordinate Ocean Model (HYCOM). *Ocean Modelling*, **7**, 285–322.

Hogg., A. McC., and J. R. Blundell, 2006: Interdecadal Variability of the Southern Ocean. *J. Phys. Oceanogr.*, **36**, 1626–1645.

Hurlburt, H. E., and P. J. Hogan, 2008: The Gulf Stream pathway and the impacts of the eddy-driven abyssal circulation and the Deep Western Boundary Current. *Dyn. Atmos. Ocean.*, **45**, 71–101.

Hurlburt, H. E., E. J. Metzger, P. J. Hogan, C. E. Tilburg, and J. F. Shriver, 2008: Steering of upper ocean currents and fronts by the topographically constrained abyssal circulation. *Dyn. Atmos. Ocean.*, **45**, 102–134.

Kallberg, P., A. Simmons, S. Uppala, and M. Fuentes, 2004: The ERA-40 Archive, ERA-40 Project Report Series No. 17, ECMWF.

Kelly, K. A., L. Thompson, W. Cheng, and E. J. Metzger, 2007: Evaluation of HYCOM in the Kuroshio Extension region using new metrics. *J. Geophys. Res.-Oceans*, **112**, C01004.

LaCasce, J H., and K. H. Brink, 2000: Geostrophic turbulence over a slope. *J. Phys. Oceanogr.*, **30**, 1305–1324.

Large, W. G., J. C. McWilliams, and S. C. Doney, 1994: Oceanic vertical mixing: a review and a model with a nonlocal boundary layer parameterization. *Rev. Geophys.*, **32**, 363–403.

Larichev, V. D., and I. M. Held, 1995: Eddy amplitudes and fluxes in a homogeneous model of fully developed baroclinic instability. *J. Phys. Oceanogr.*, **25**, 2285–2297.

Merryfield, W. J., 1998: Effects of stratification on quasi-geostrophic inviscid equilibria. *J. Fluid Mech.*, **354**, 345–356.

Nadeau, L.-P., and D. N. Straub, 2012: Influence of wind stress, wind stress curl, and bottom friction on the transport of a model Antarctic Circumpolar Current. *J. Phys. Oceanogr.*, **42**, 207–222.

Nadeau, L.-P., D. N. Straub, and D. M. Holland, 2013: Comparing idealized and complex topographies in quasigeostrophic simulations of an Antarctic Circumpolar Current. *J. Phys. Oceanogr.*, **43**, 1821–1837.

Nadeau, L.-P., and R. Ferrari, 2015: The role of closed gyres in setting the zonal transport of the Antarctic Circumpolar Current. *J. Phys. Oceanogr.*, **45**, 1491–1509.

Naveira-Garabato, A. C., A. J. G. Nurser, R. B. Scott, and J. A. Goff, 2013: The impact of small-scale topography on the dynamical balance of the ocean. *J. Phys. Oceanogr.*, **43**, 647–668.

Nikurashin, M., and R. Ferrari, 2011: Global energy conversion rate from geostrophic flows into internal lee waves in the deep ocean, *Geophys. Res. Lett.*, **38**, L08610.

Olbers, D. D. Borowski, C. Völker, and J.-O. Wolff, 2004: The dynamical balance, transport and circulation of the Antarctic Circumpolar Current. *Antarctic Science*, **16**(4), 439–470.

Özgökmen, T., and E. P. Chassignet, 1998: Emergence of inertial gyres in a two-layer quasi-geostrophic model. *J. Phys. Oceanogr.*, **28**, 461–484.

Qiu, B., R. B. Scott, and S. Chen, 2008: Length scales of eddy generation and nonlinear evolution of the seasonally modulated South Pacific Subtropical Countercurrent. *J. Phys. Oceanogr.*, **38**, 1515–1528.

Radko, T., D. Peixoto de Carvalho, and J. Flanagan, 2014: Nonlinear equilibration of baroclinic instability: the growth rate balance model. *J. Phys. Oceanogr.*, **44**, 1919–1940.

Rhines, P. B, 1970: Edge-, bottom-, and Rossby waves in a rotating stratified fluid. *Geophys. Fluid Dyn.*, **1**, 273–302.

Rhines, P., 1977: The dynamics of unsteady currents. Vol. 6, *The Sea*, Interscience, 189–318.

Riviere, P., A. M. Treguier, and P. Klein, 2004: Effects of bottom friction on nonlinear equilibration of an oceanic baroclinic jet. *J. Phys. Oceanogr.*, **34**, 416–432.

Rosmond, T. E., J. Teixeira, M. Peng, T. F. Hogan, and R. Pauley, 2002: Navy Operational Global Atmospheric Prediction System (NOGAPS): forcing for ocean models. *Oceanography*, **15**, 99–108.

Salmon, R., 1978: Two-layer quasi-geostrophic turbulence in a simple special case. *Geophys. Astrophys. Fluid Dyn.*, **10**, 25–52.

Salmon, R., 1980: Baroclinic instability and geostrophic turbulence. *Geophys. Astrophys. Fluid Dyn.*, **15**, 167–211.

Schlösser, F., and C. Eden, 2007: Diagnosing the energy cascade in a model of the North Atlantic. *Geophys. Res. Lett.*, **34**, L02604, doi:10.1029/2006GL027813.

Scott, R. B., and F. Wang, 2005: Direct evidence of an oceanic inverse kinetic energy cascade from satellite altimetry. *J. Phys. Oceanogr.*, **35**, 1650–1666, doi:10.1175/JPO2771.1.

Scott, R. B., and B. K. Arbic, 2007: Spectral energy fluxes in geostrophic turbulence: Implications for ocean energetics. *J. Phys. Oceanogr.*, **37**, 673–688, doi:10.1175/JPO3027.1.

Scott, R. B., B. K. Arbic, E. P. Chassignet, A. C. Coward, M. Maltrud, W. J. Merryfield, A. Srinivasan, and A. Varghese, 2010: Total kinetic energy in four global eddying ocean circulation models and over 5000 current meter records. *Ocean Modelling*, **32**, 157–169.

Scott, R. B., J. A. Goff, A. C. Naveira-Garabato, and A. J. G. Nurser, 2011: Global rate and spectral characteristics of internal gravity wave generation by geostrophic flow over topography, *J. Geophys. Res.*, **116**, C09029, doi:10.1029/2011JC007005.

Sen, A., R. B. Scott, and B. K. Arbic, 2008: Global energy dissipation rate of deep-ocean low-frequency flows by quadratic bottom boundary layer drag: computations from current-meter data. *Geophys. Res. Lett.*, **35**, L09606, doi:10.1029/2008GL033407.

Sinha, B., and K. J. Richards, 1999: Jet structure and scaling in Southern Ocean models. *J. Phys. Oceanogr.*, **29**, 1143–1155.

Smagorinsky, J., 1993: Large eddy simulation of complex engineering and geophysical flows, in *Evolution of Physical Oceanography*, edited by B. Galperin, and S. A. Orszag, pp. 3–36. Cambridge University Press.

Smith, W. H. F., and D. T. Sandwell, 1997: Global seafloor topography from satellite altimetry and ship depth soundings. *Science*, **277**, 1957–1962.

Srinivasan, A., Z. Garraffo, and M. Iskandarani, 2009: Abyssal circulation in the Indian Ocean from a 1/12^{o} resolution global hindcast. *Deep-Sea Res. I*, **56**, 1907–1926.

Stammer, D., 1997: Global characteristics of ocean variability estimated from regional TOPEX/Poseidon altimeter measurements. *J. Phys. Oceanogr.*, **27**, 1743–1769.

Stewart, K. D., J. A. Saenz, A. McC. Hogg, G. O. Hughes, and R. W. Griffiths, 2014: Effect of topographic barriers on the rates of available potential energy conversion of the oceans. *Ocean Modelling*, **76**, 31–42.

Straub, D. N., and B. T. Nadiga, 2014: Energy fluxes in the quasigeostrophic double gyre problem. *J. Phys. Oceanogr.*, **44**, 1505–1522.

Taylor, G. I., 1919: Tidal friction in the Irish Sea. *Philos. Trans. R. Soc. London, Ser. A*, *220*, 1–33.

Thompson, A. F., 2010: Jet formation and evolution in baroclinic turbulence with simple topography. *J. Phys. Oceanogr.*, **40**, 257–278.

Thompson, A. F., and W. R. Young, 2006: Scaling baroclinic eddy fluxes: vortices and energy balance. *J. Phys. Oceanogr.*, **36**, 720–738.

Thoppil, P. G., J. G. Richman, and P. J. Hogan, 2011: Energetics of a global ocean circulation model compared to observations. *Geophys. Res. Lett.*, **38**, L15607, doi:10.1029/2011GL048347.

Timko, P. G., B. K. Arbic, J. G. Richman, R. B. Scott, E. J. Metzger, and A. J. Wallcraft, 2013: Skill testing a three-dimensional global tide model to historical current meter records. *J. Geophys. Res.-Oceans*, **118**, 6914–6933, doi:10.1002/2013JC009071.

Treguier, A. M., and B. L. Hua, 1988: Influence of bottom topography on stratified quasi-geostrophic turbulence in the ocean. *Geophys. Astrophys. Fluid Dyn.*, **43**, 265–305.

Treguier, A. M., and J. C. McWilliams, 1990: Topographic influences on wind-driven, stratified flow in a β-plane channel: An idealized model for the Antarctic Circumpolar Current. *J. Phys. Oceanogr.*, **20**, 321–343.

Trossman, D. S., B. K. Arbic, S. T. Garner, J. A. Goff, S. R. Jayne, E. J. Metzger, and A. J. Wallcraft, 2013: Impact of parameterized lee wave drag on the energy budget of an eddying global ocean model. *Ocean Modelling*, **72**, 119–142.

Trossman, D. S., S. Waterman, K. L. Polzin, B. K. Arbic, S. T. Garner, A. C. Naveira-Garabato, and K. L. Sheen, 2015: Internal lee wave closures: parameter sensitivity and comparison to observations. *J. Geophys. Res.-Oceans*, **120**, doi:10.1002/2015JC010892.

Trossman, D. S., B. K. Arbic, J. G. Richman, S. T. Garner, S. R. Jayne, and A. J. Wallcraft, 2016: Impact of topographic internal lee wave drag on an eddying global ocean model. *Ocean Modelling*, **97**, 109–128.

Trowbridge, J. H., W. R. Geyer, M. M. Bowen, and A. J. Williams, 1999. Near-bottom turbulence measurements in a partially mixed estuary: turbulent energy balance, velocity structure, and along-channel momentum balance. *J. Phys. Oceanogr.*, **29**, 3056–3072

Trowbridge, J., and S. Elgar, 2001: Turbulence measurements in the surf zone. *J. Phys. Oceanogr.*, **31**, 2403–2417.

Tulloch, R., J. Marshall, C. Hill, and K. S. Smith, 2011: Scales, growth rates, and spectral fluxes of baroclinic instability in the ocean. *J. Phys. Oceanogr.*, **41**, 1057–1076.

Uppala, S. M., P. W. Kallberg, A. J. Simmons, U. Andrae, V. Da Costa Bechtold, M. Fiorino, J. K. Gibson, J. Haseler, A. Hernandez, G. A. Kelly, X. Li, K. Onogi, S. Saarinen, N. Sokka, R. P. Allan, E. Andersson, K. Arpe, M. A. Balmaseda, A. C. M. Beljaars, L. Van De Berg, J. Bidlot,

N. Bormann, S. Caires, F. Chevallier, A. Dethof, M. Dragosavac, M. Fisher, M. Fuentes, S. Hagemann, E. Holm, B. J. Hoskins, L. Isaksen, P. A. E. M. Janssen, R. Jenne, A. P. Mcnally, J.-F. Mahfouf, J.-J. Morcrette, N. A. Rayner, R. W. Saunders, P. Simon, A. Sterl, K. E. Trenberth, A. Untch, D. Vasiljevic, P. Viterbo, and J. Woollen, 2005: The ERA-40 renalaysis. *Q. J. R. Meteorol. Soc.*, **131**, 2961–3012, doi:10.1256/qj.04.176.

Venaille, A., G. K. Vallis, and K. S. Smith, 2011: Baroclinic turbulence in the ocean: analysis with primitive equation and quasigeostrophic simulations. *J. Phys. Oceanogr.*, **41**, 1605–1623.

Venaille, A., 2012: Bottom-trapped currents as statistical equilibrium states above topographic anomalies. *J. Fluid Mech.*, **699**, 500–510.

Weatherly, G. L., 1975: A numerical study of time-dependent turbulent Ekman layers over horizontal and sloping bottoms. *J. Phys. Oceanogr.*, **5**, 288–299.

Willebrand, W., B. Barnier, C. Boning, C. Dieterich, P. D. Killworth, C. Le Provost, Y. Jia, J.-M. Molines, and A. L. New, 2001: Circulation characteristics in three eddy-permitting models of the North Atlantic, *Progr. Oceanogr.*, **48**, 123–161.

Wright, C. J., R. B. Scott, D. Furnival, P. Ailliot, and F. Vermet, 2013: Global Observations of Ocean-Bottom Subinertial Current Dissipation, *J. Phys. Oceanogr.*, **43**, 402–417.

Wright, C. J., R. B. Scott, P. Ailliot, and D. Furnival, 2014: Lee wave generation rates in the deep ocean, *Geophys. Res. Lett.*, **41**; doi:10.1002/2013GL059087.

Wunsch, C., 1997: The vertical partition of oceanic horizontal kinetic energy. *J. Phys. Oceanogr.*, **27**, 1770–1794.

Xu, X., P. B. Rhines, and E. P. Chassignet, 2016: Temperature-salinity structure of the North Atlantic circulation and associated heat and freshwater transports. *J. Clim.*, doi:10.1175/JCLI-D-15-0798.1.

LIST OF TABLES

TABLE 1. Horizontal resolutions, nondimensional drag coefficient (C_d) values, and barotropic and baroclinic time steps (t_{BT} and t_{BC}, respectively, each given in seconds) for the $1/25^o$ global and $1/12^o$ Atlantic HYCOM simulations analyzed in this manuscript.

Resolution	global/regional	wave drag?	C_d	t_{BT}	t_{BC}
$1/12^o$	Atlantic	no	2.5×10^{-3} (mid)	7.5	120
$1/12^o$	Atlantic	no	5.0×10^{-4} (weak)	7.5	15
$1/25^o$	global	no	2.5×10^{-3} (mid)	2	120
$1/25^o$	global	no	2.5×10^{-1} (strong)	2	40
$1/25^o$	global	yes	2.5×10^{-3} (wave drag)	2	20

TABLE 2. The area-weighted average of the sea surface height (SSH) variance [m^2] and geostrophic surface kinetic energy (SKE) [$m^2\ s^{-2}$] fields from the $1/25^o$ global and $1/12^o$ Atlantic HYCOM simulations.

Resolution	global/regional	wave drag?	C_d	SSH variance	geostrophic SKE
$1/12^o$	Atlantic	no	2.5×10^{-3} (mid)	0.0079	0.0314
$1/12^o$	Atlantic	no	2.5×10^{-4} (weak)	0.0068	0.0311
$1/25^o$	global	no	2.5×10^{-3} (mid)	0.0083	0.0075
$1/25^o$	global	no	2.5×10^{-1} (strong)	0.0089	0.0076
$1/25^o$	global	yes	2.5×10^{-3} (wave drag)	0.0068	0.0063

TABLE 3. The ratio of the total KE in the top 100 meters (KE_{top100}) to total KE in the bottom 500 meters (KE_{bot500}) from the regional $1/12^o$ HYCOM and global $1/25^o$ HYCOM simulations. Grid points within 30 indices of the coasts were excluded from this calculation due to the occurrence of infinitesimal layer thicknesses. The asterisk (*) indicates that KE_{top100} was not saved; instead, the geostrophic SKE is used.

global/regional	wave drag?	C_d	KE_{top100}/KE_{bot500}
regional	no	2.5×10^{-3}	18.5
regional	no	5.0×10^{-4}	3.51
global	no	2.5×10^{-3}	16.1
global	no	2.5×10^{-1}	41.8
global	yes	2.5×10^{-3}	51.1*

TABLE 4. The domain-integrated kinetic energy (E_{tot}) [GJ$= 10^9$J] in the quasi-geostrophic (QG) basin simulations with a flat bottom and rough bottom topography for three different values of linear bottom drag coefficients. The units of r_{QG} are in s^{-1}.

flat/rough topography	r_{QG}	E_{tot}
flat bottom	8×10^{-10}	750
flat bottom	8×10^{-8}	66
flat bottom	8×10^{-6}	48
rough bottom	8×10^{-10}	91
rough bottom	8×10^{-8}	53
rough bottom	8×10^{-6}	46

TABLE 5. The surface eddy horizontal length scales (L_{KE}) (units in km) associated with geostrophic surface kinetic energy computed over the final year of the $1/25^o$ global HYCOM simulations and $1/12^o$ Atlantic HYCOM simulations. The domain chosen for the entries listed here is the North Atlantic between $59.3^o - 39.3^o$W and $19.6^o - 39.6^o$N, very close to the region shown in Fig. 1.

configuration	C_d	wave drag?	L_{KE}
$1/12^o$ Atlantic	5×10^{-4}	no	50.4
$1/12^o$ Atlantic	2.5×10^{-3}	no	52.0
$1/25^o$ global	2.5×10^{-3}	no	56.7
$1/25^o$ global	2.5×10^{-1}	no	53.8
$1/25^o$ global	2.5×10^{-3}	yes	51.4

LIST OF FIGURES

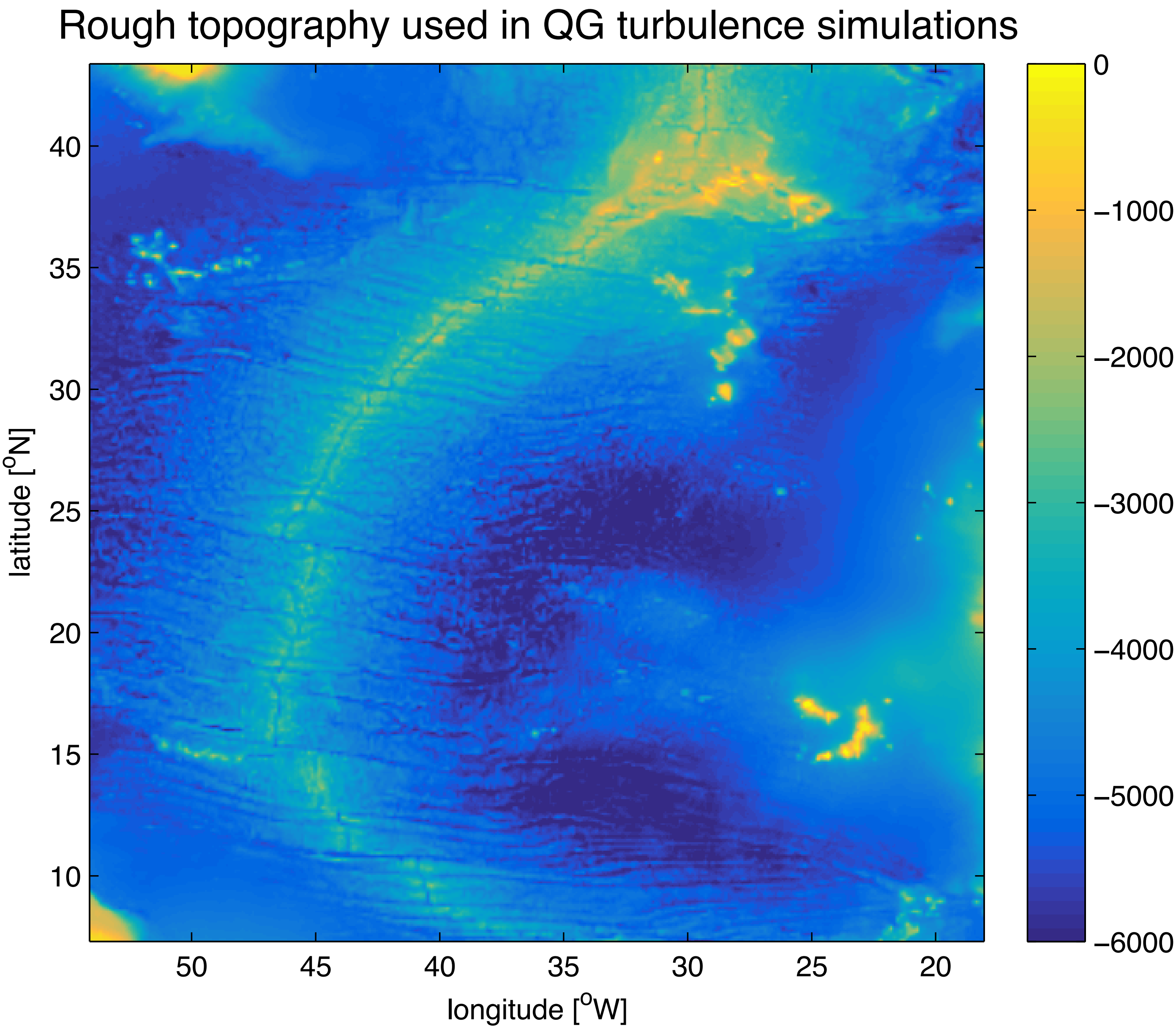

FIG. 1. The rough bottom topography used in the QG basin simulations. The colorbar values are given in units of meters below the sea surface. The minimum depth is greater than 10 meters.

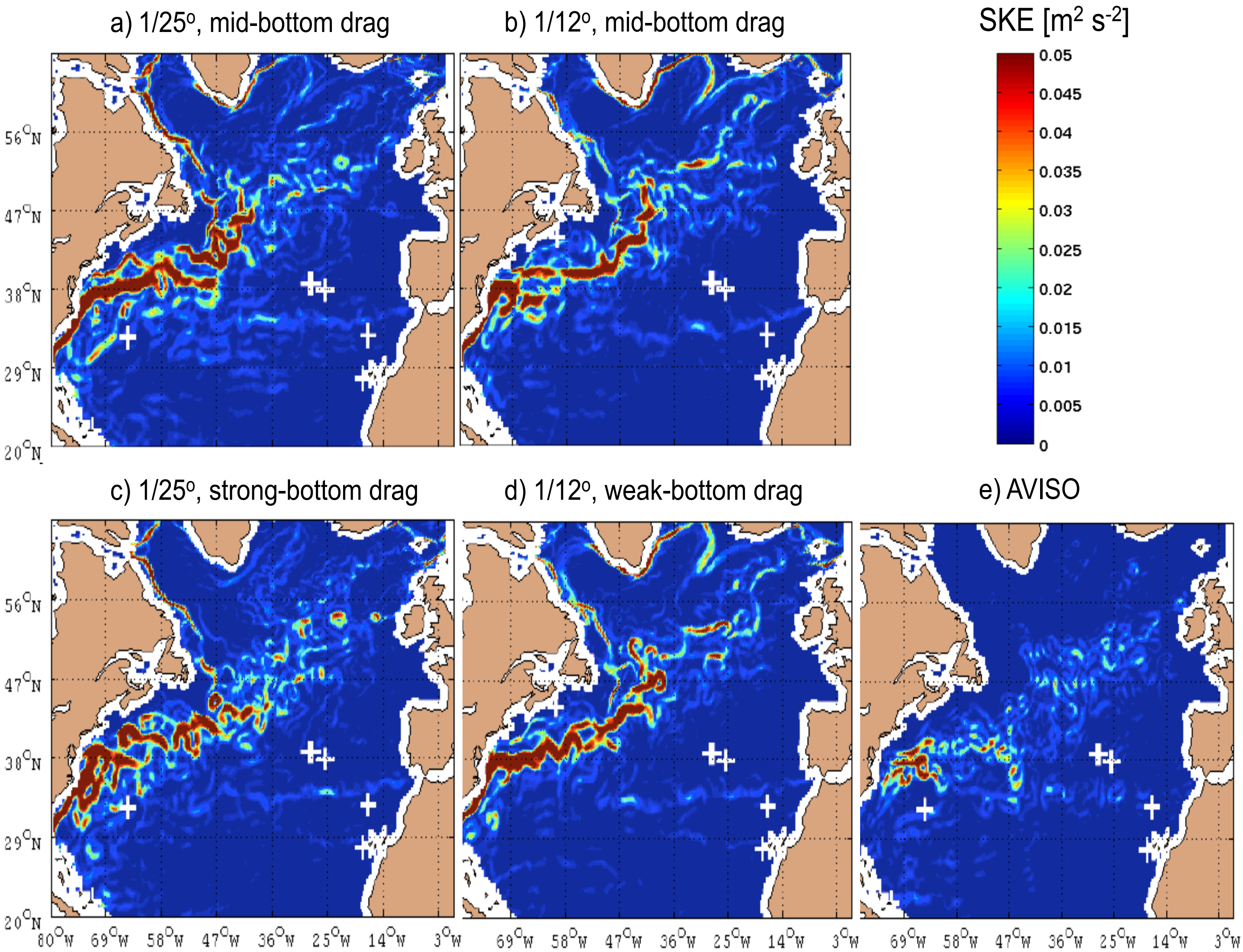

FIG. 2. Shown are the time-averaged geostrophic surface kinetic energies (SKE; units in $m^2\ s^{-2}$) in the North Atlantic, computed using a nine-point stencil (*Arbic et al.* 2012) from the final year of (a) the mid-bottom drag $1/25^o$ global HYCOM simulation, (c) the strong-bottom drag $1/25^o$ global HYCOM simulation, (b) the mid-bottom drag $1/12^o$ Atlantic HYCOM simulation, (d) the weak-bottom drag $1/12^o$ Atlantic HYCOM simulation, and (e) over all years (1992 – 2008) of AVISO data.

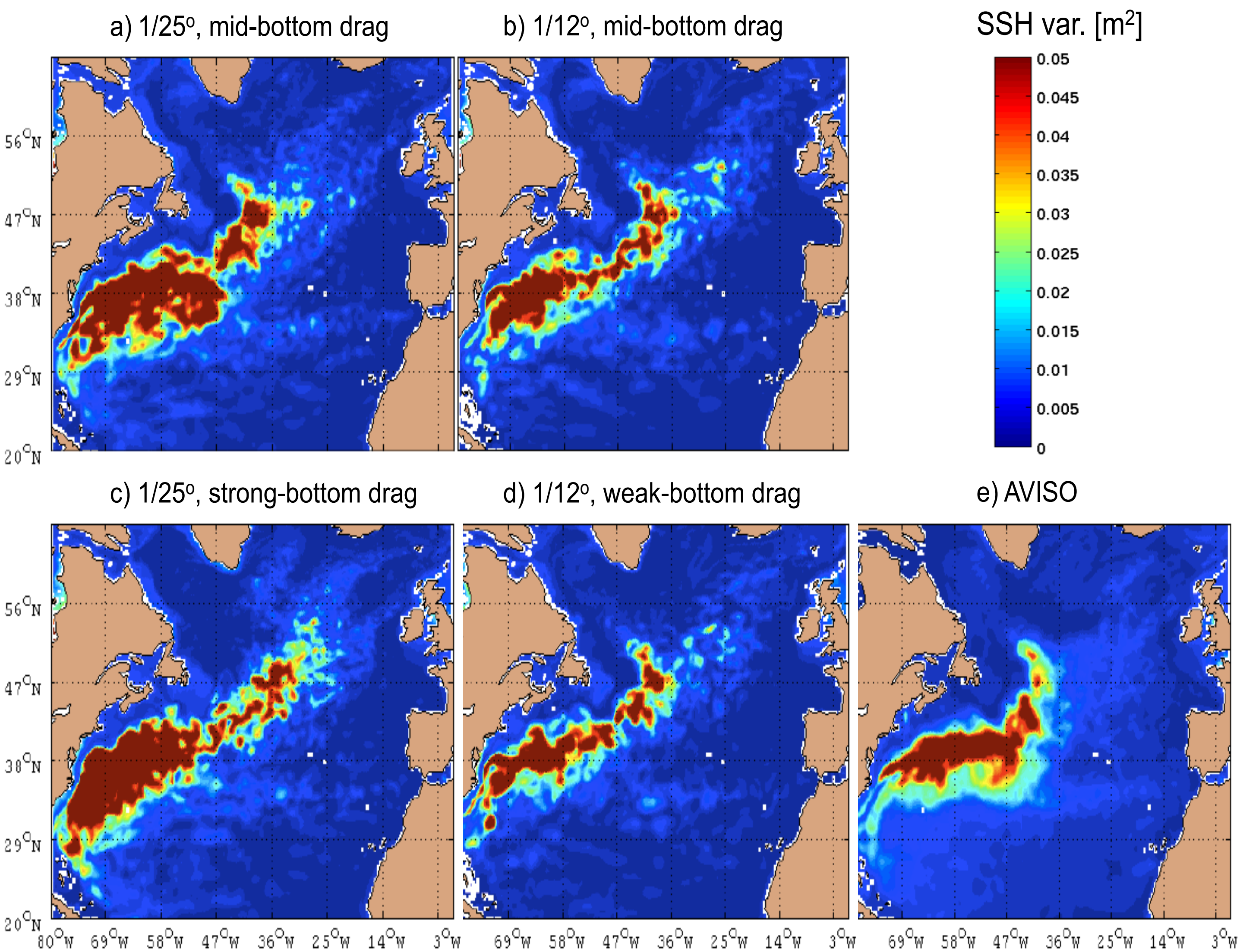

890 FIG. 3. Shown are the sea surface height (SSH) variances (units in m^2) in the North Atlantic, averaged over
891 the final year of (a) the mid-bottom drag $1/25^o$ global HYCOM simulation, (c) the strong-bottom drag $1/25^o$
892 global HYCOM simulation, (b) the mid-bottom drag $1/12^o$ Atlantic HYCOM simulation, (d) the weak-bottom
893 drag $1/12^o$ Atlantic HYCOM simulation, and (e) over all years $(1992-2008)$ of AVISO data.

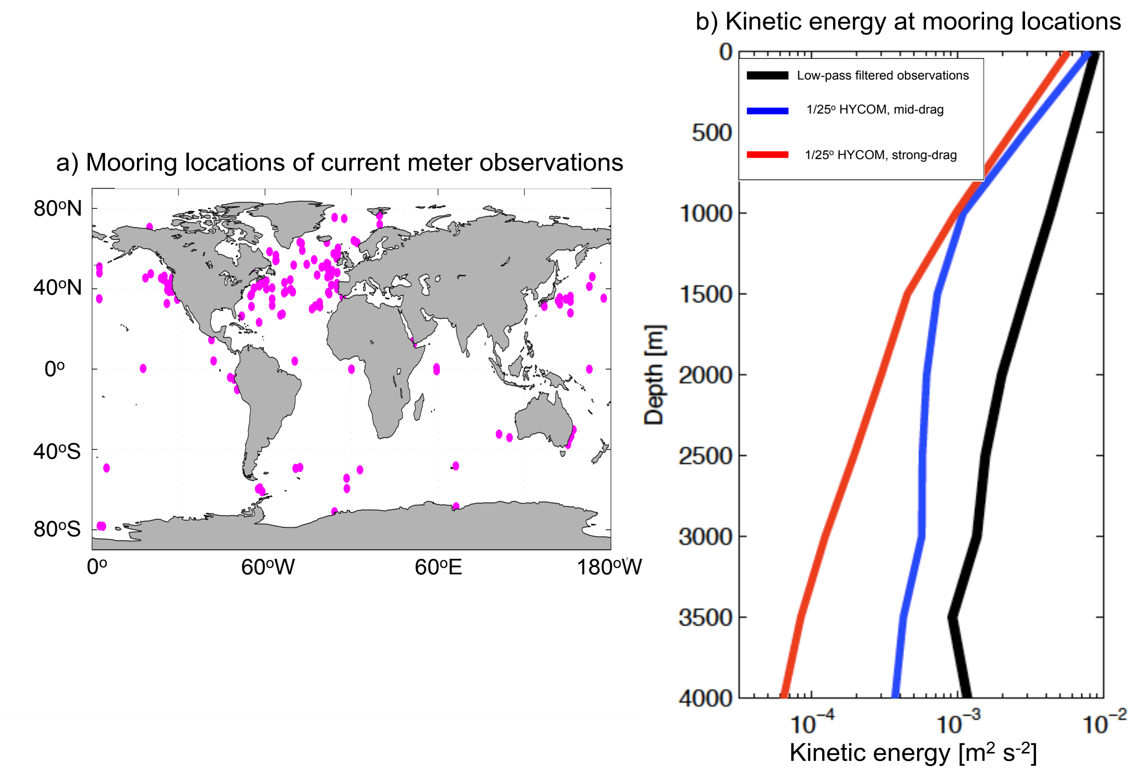

FIG. 4. (a) The horizontal locations (magenta circles) of the current meter observations used in this study. (b) The geometric averages (solid curves) of the kinetic energy profiles over all of these horizontal locations. Panel b employs daily-averaged output of the strong-bottom drag $1/25^o$ global HYCOM simulation (red), mid-bottom drag $1/25^o$ global HYCOM simulation (blue), and low-pass filtered current meter observations (black).

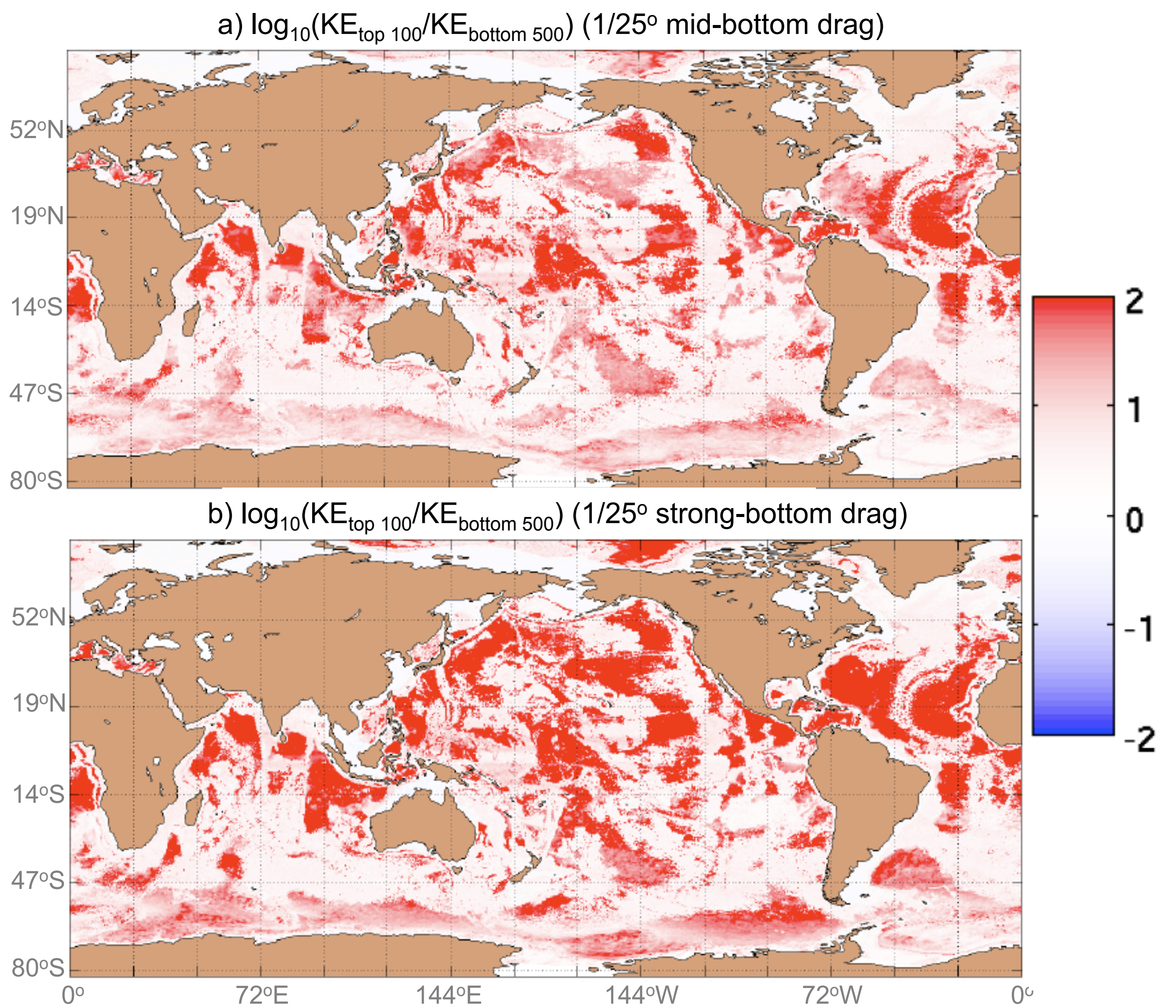

FIG. 5. Shown are the base-10 logarithms of the ratios of the kinetic energy (KE) averaged over the top 100 meters to that averaged over the bottom 500 meters, each computed as a time average over the final year of (a) the mid-bottom drag $1/25^o$ global HYCOM simulation and (b) the strong-bottom drag $1/25^o$ global HYCOM simulation.

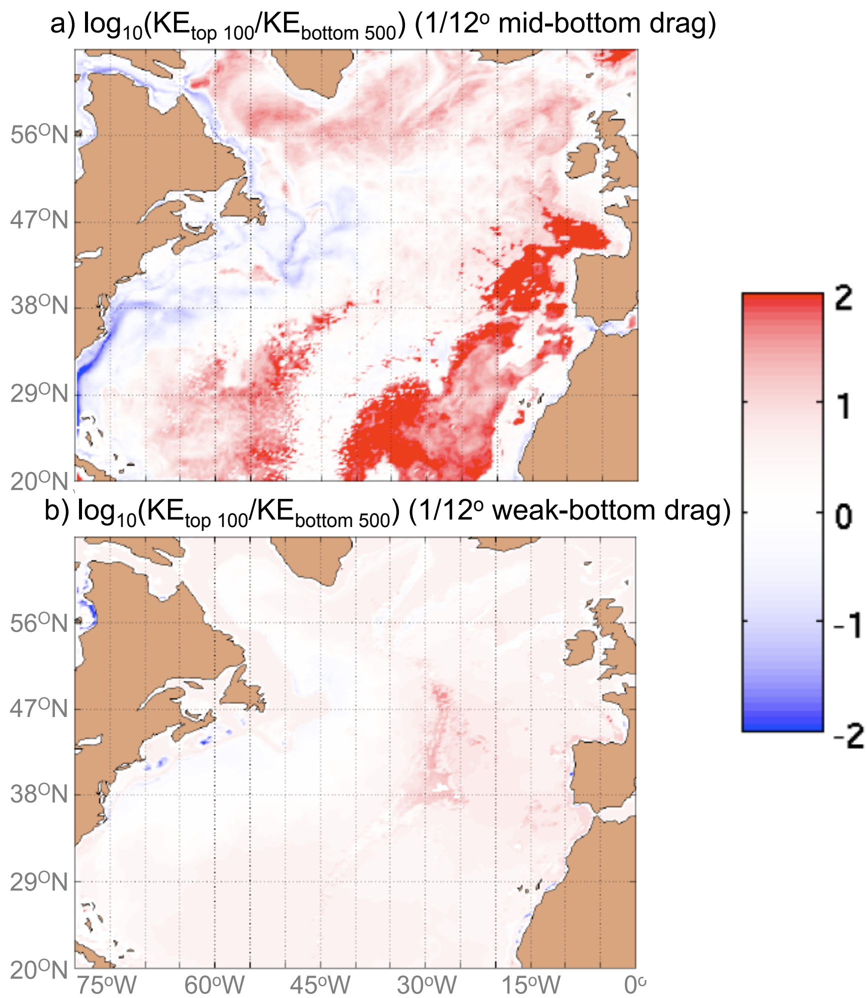

FIG. 6. Shown are the base-10 logarithms of the ratios of the kinetic energy (KE) averaged over the top 100 meters to that averaged over the bottom 500 meters, each computed as a time average over (a) the final year of the mid-bottom drag $1/12^{o}$ Atlantic HYCOM simulation and (b) the weak-bottom drag $1/12^{o}$ Atlantic HYCOM simulation.

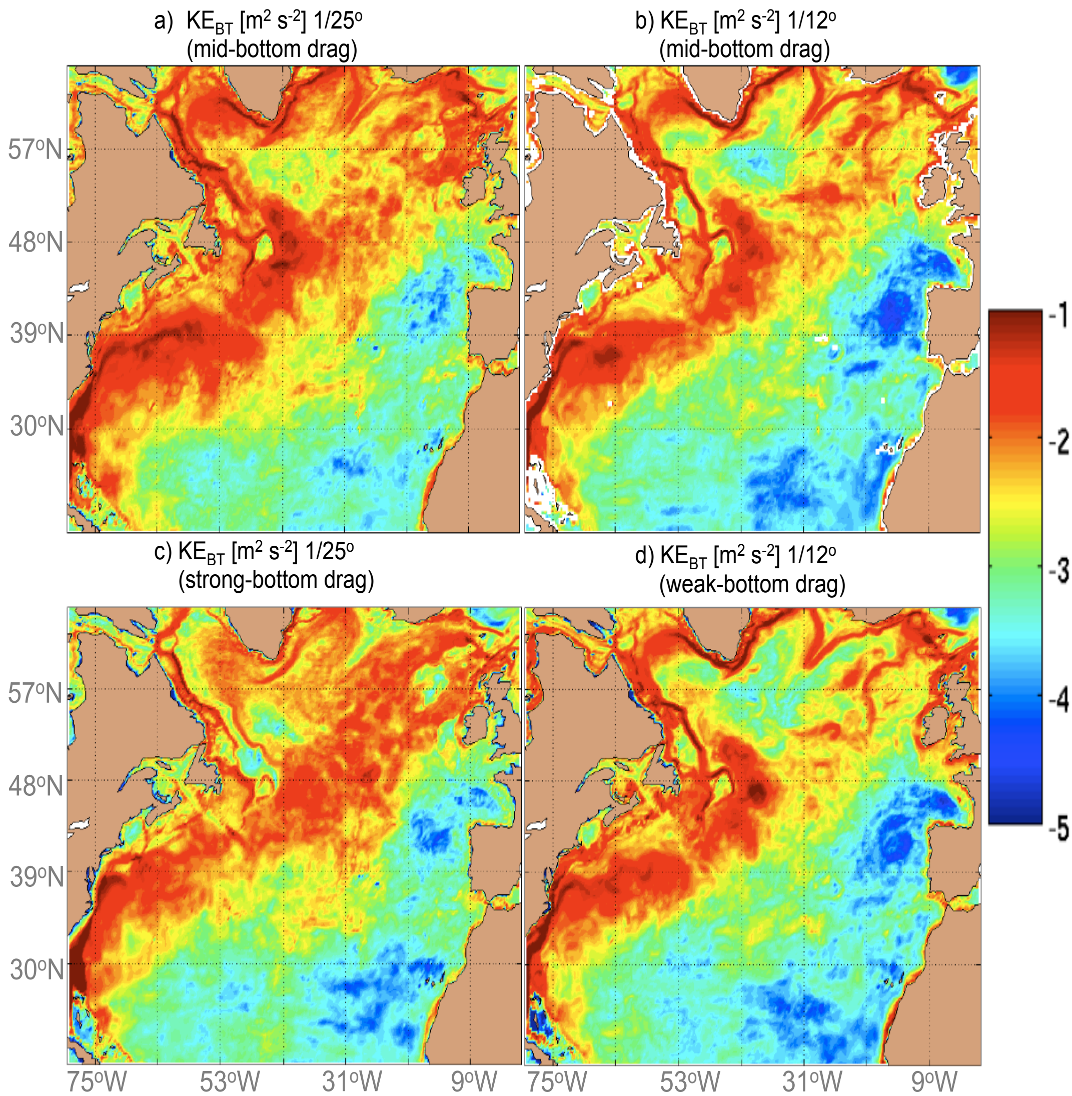

FIG. 7. Shown is the base-10 logarithm of the barotropic kinetic energy, KE_{BT} (units in m^2 s^{-2}), averaged over the final year of (a) the mid-bottom drag $1/25^o$ global HYCOM simulation, (c) the strong-bottom drag $1/25^o$ global HYCOM simulation, (b) the mid-bottom drag $1/12^o$ Atlantic HYCOM simulation, and (d) the weak-bottom drag $1/12^o$ Atlantic HYCOM simulation.

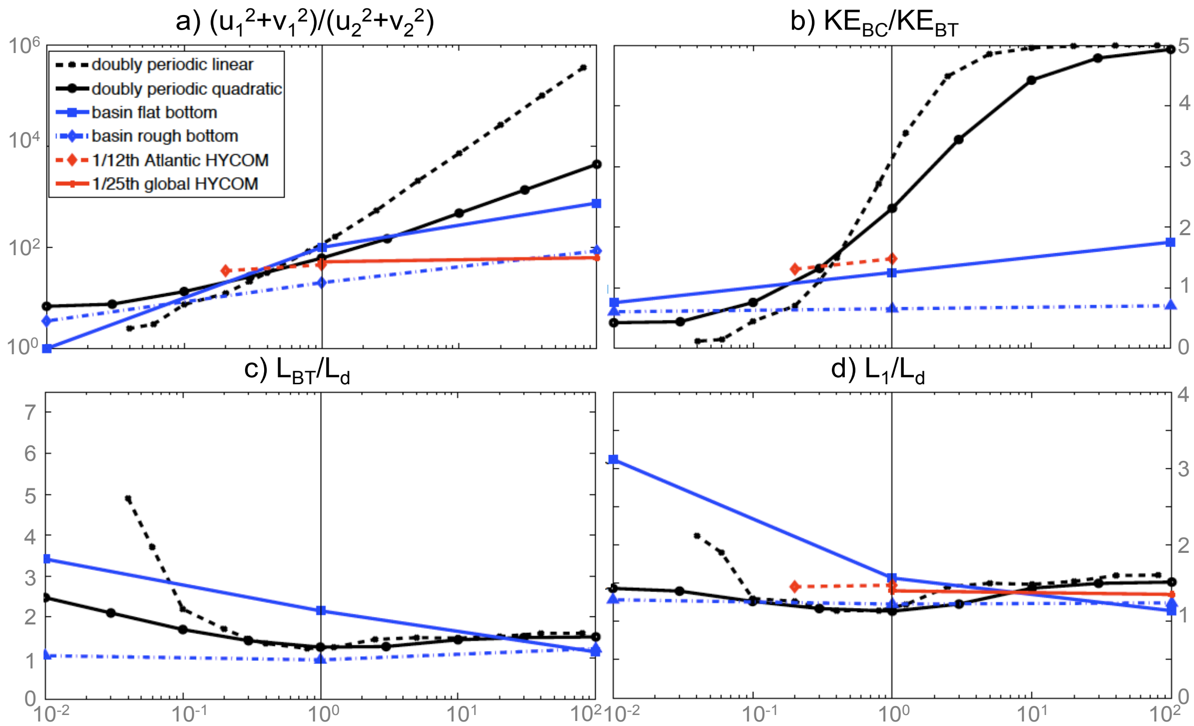

FIG. 8. Shown are results from the horizontally homogeneous, two-layer, flat-bottom, f-plane, doubly periodic QG turbulence simulations with linear and quadratic bottom drags from *Arbic and Flierl* (2004) and *Arbic and Scott* (2008); the QG β-plane basin simulations with a flat bottom and rough bottom topography; and the $1/12^o$ Atlantic and $1/25^o$ global HYCOM simulations. We show non-dimensional eddy statistics: (a) the ratio of the domain-averaged kinetic energy (KE) in the top layer (subscript 1) to that in the bottom layer (subscript 2), (b) the domain-averaged ratio of the baroclinic KE to barotropic KE, (c) the domain-averaged ratio of the eddy length scales associated with KE in the barotropic mode (L_{BT}) to the Rossby radius of deformation (L_d), and (d) the domain-averaged ratio of the eddy length scales associated with KE in the upper layer (L_1) to L_d. A domain average has been taken over a region (between $59.3^o - 39.3^o$W and $19.6^o - 39.6^o$N) very close to the one shown in Fig. 1 for the $1/12^o$ Atlantic and $1/25^o$ global HYCOM simulations. Over this domain, L_d is assumed to be 30 km for not only the QG simulations, but also for the HYCOM simulations. The abscissa in each panel shows the nondimensional friction, as defined by *Arbic and Scott* (2008) for the doubly periodic QG simulations, and as defined by the relative magnitude of C_d or r_{QG}, with respect to the control simulation, for the HYCOM and QG basin simulations.

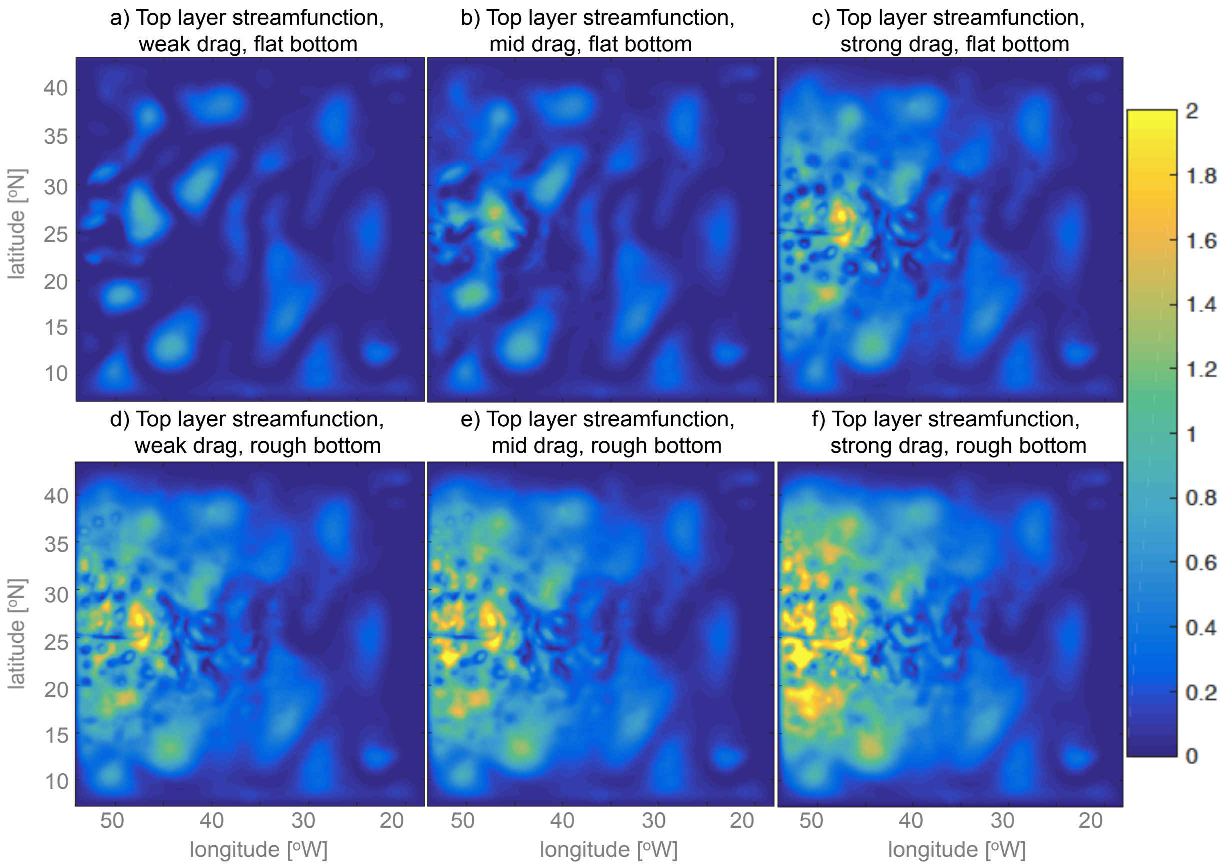

922 FIG. 9. Shown are representative snapshots of the streamfunction (units in $\mathrm{m}^2\ \mathrm{s}^{-1}$) in the top layer of the QG
923 β-plane basin simulations with (a-c) a flat bottom and (d-f) rough bottom topography. The simulations use a
924 linear bottom drag coefficient of (a,d) $8\times10^{-10}\ \mathrm{s}^{-1}$, (b,e) $8\times10^{-8}\ \mathrm{s}^{-1}$, and (c,f) $8\times10^{-6}\ \mathrm{s}^{-1}$. The axes have
925 the same latitude and longitude labels as in Fig. 1.

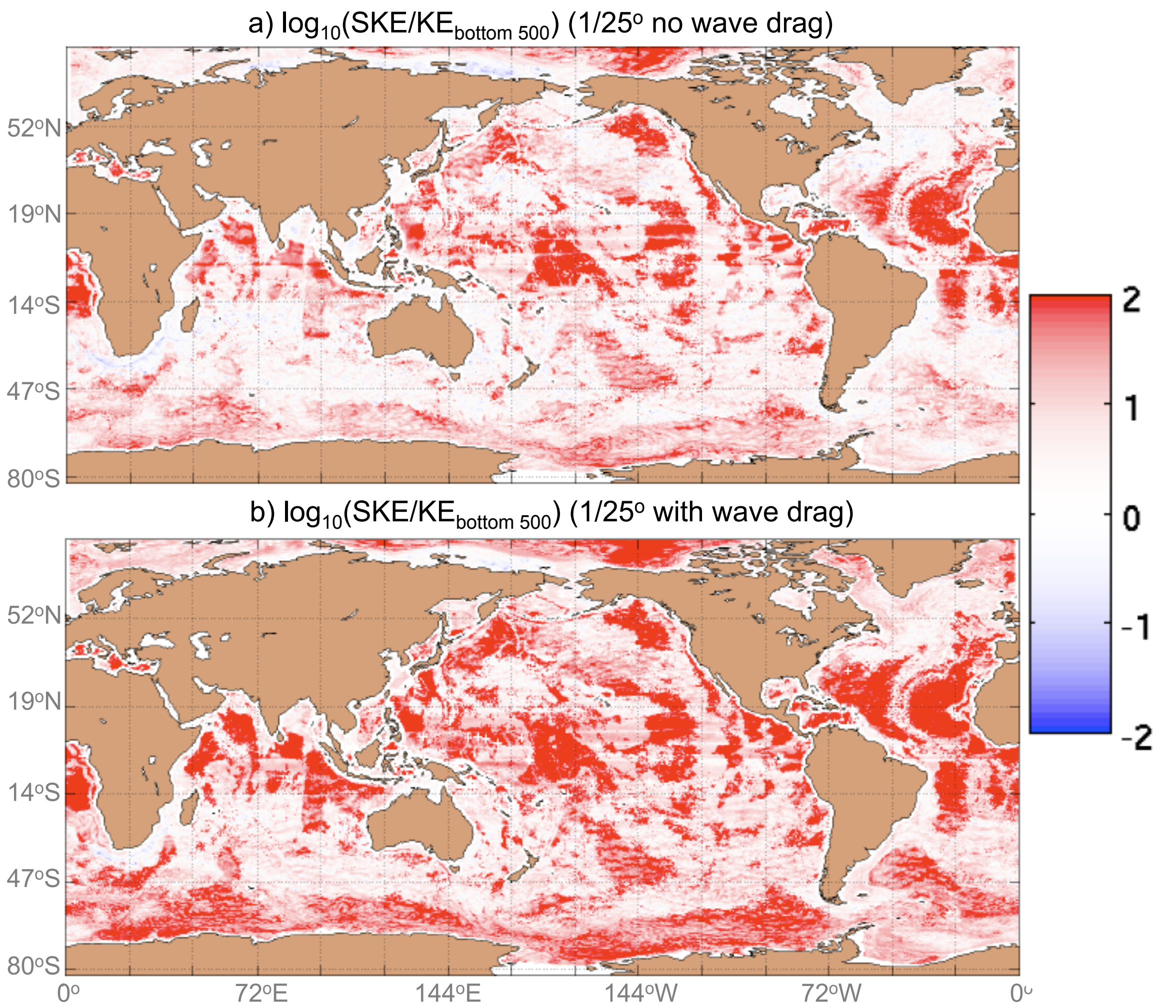

FIG. 10. Shown are the base-10 logarithms of the ratios of the geostrophic surface kinetic energy (KE) to the KE averaged over the bottom 500 meters, each computed as a time average over the final year of (a) the mid-bottom drag $1/25^o$ global HYCOM simulation without wave drag and (b) the $1/25^o$ global HYCOM simulation with wave drag.